WESTERN REGION TECHNICAL ATTACHMENT
NO. 99-18
AUGUST 31, 1999

AN OBSERVATIONAL STUDY OF ISLAND EFFECT BANDS: PRECIPITATION PRODUCERS IN SOUTHERN CALIFORNIA

Ivory J. Small - NWSO San Diego, CA

[Note: All figures and tables appear on the web page only.]

Introduction

The topic of low-level flow interacting with varying terrain to produce precipitation is not new, but continues to be a forecasting challenge, especially in the West. Some well-known, low-level flow/terrain interactions are the Puget Sound Convergence Zone (Whitney et al. 1993) in northwest Washington State, and the Denver Convergence-Vorticity Zone (Szoke et al. 1984) in Colorado. These are locations where, under certain conditions, mesoscale convergence zones develop.

In the Bight Region of southern California (Fig. 1), there is a very significant flow/terrain interaction that can result in the production of showers and even thunderstorms over the coastal waters and locally inland over the coastal and inland areas. They appear to be lines of enhanced convection which form due to flow over and around the offshore islands resulting in convergence/confluence zones extending downwind. Frequently there is a cloud-free zone between the bands, downwind from the island. These bands of showers and thunderstorms appear to develop in an environment very similar to the environments that can result in lake-effect snow (Agee and Hart 1990), and lake-effect rain (Miner and Fritsch 1997) events. The bands form well in a post-frontal environment, when the synoptic scale pressure gradient is west to east due to lower pressure inland (west to east pressure gradient is known locally as an *onshore pressure gradient, and the associated west to east low-level flow is known as onshore flow*). There are many similarities between these bands created by the islands, and lake-effect events. Based primarily on the similarities between these bands created by the islands and bands formed during lake-effect events, the phenomena have been called the "Island Effect" by forecasters in southwestern California. This "Island Effect", simply identified as "IE" from this point forward, can be defined as follows:

The development of one or more cloud bands downwind from an island where the bands are:

1. Formed as a result of the influence of the island on the flow.
2. Frequently enhanced in comparison to other bands in the area.
3. Often found with one or more cloud-free zones associated with them.

Frequently, when IE bands develop, mesoscale cellular convection is visible over the ocean, over the land, or both.

In order to examine these phenomena, in section II a discussion of low-level flow using the Froude number will be given. In section III some background theory concerning convection over large bodies of water will be presented. In section IV the conditions associated with lake-effect rain events in Minor and Fritsch (1997) will be examined. In section V, 10 case studies in southern California will be presented for comparison. In section VI a list of the conditions that frequently result in IE bands, along with additional discussion and conclusions will be made, coupled with some final thoughts on the importance of understanding these phenomena.

Variations in the Froude Number and its Effect on Low-level Flow

It is instructive to consider the Froude number when observing low-level flow/terrain interactions. A good source of information concerning Froude number for the California bight is in Clark and Dembek (1991).

$Fr = U/Nh$

where

U = mean wind speed
N = buoyancy frequency
h = terrain height

As can be seen from the equation, when the low-level winds decrease or the static stability increases, the Froude number decreases. Lower Froude numbers (approximately equal to 1 or less) result in enhanced blocking by topography. Clark and Dembek stated that airstreams incident upon topography in the Catalina Eddy case probably cannot be characterized by a single value of Froude number. For instance, the lowest levels of the incident airstream might have values less than 0.5 because of the small wind speed, whereas higher levels might have values greater than 0.5. (The same is likely to be true for the convergence zones created by blocked flow associated with the islands as well as the mainland terrain during post-frontal situations). They suggested that simulations with high-resolution multi-level models might be needed to fully examine terrain blocking

associated with the eddy. That was beyond the scope of their paper, as the case here. This Technical Attachment (TA) is meant to be mainly a view of the boundaries from an observational standpoint. In addition to the terrain-forced boundaries, boundaries associated with mesoscale cellular convection will frequently develop during post-frontal situations. Sometimes the two can interact to enhance the convection.

Before the introduction of Doppler radar and high resolution satellite data, it was very difficult to observe these phenomena with much detail. With the installation of NEXRAD (Next Generation Weather Radar) in the Bight region, along with improved satellite data, these phenomena can now be easily observed.

Brief Overview of Convection over the Ocean

In mid-latitudes, convection over the ocean, or other very large bodies of water, is most frequently observed in the winter season when cold polar air behind a mid-latitude frontal system moves over a relatively warm ocean. The warming influence of the ocean surface is a principle mechanism for destabilizing the polar airmass by warming the lowest levels and adding moisture to the airmass. Essentially, strong fluxes of latent and sensible heat from the warmer water results in a boundary layer that is very unstable to shallow, moist convection. A good example is from the North Atlantic, and is found in Bader et al. (1995). Figures 2-4 show the typical patterns that accompany an outbreak of polar air over the warmer ocean. Figures 5 and 6 show the typical soundings associated with the points shown in the satellite imagery and schematics. At point A the cold northwest flow is still very dry, so there is no cloud development at that point. A schematic sounding for point A is shown in Fig. 5a. By the time point B and C are reached, the airmass has deepened up enough for horizontal roll convection to develop (e.g., Staudenmaier 1995; Weckwerth et al. 1997). The soundings for point B and C are shown in schematic soundings 5b and 5c, respectively. By point D, characterized the schematic sounding in Fig. 6a open cell convection has developed (Agee et al.1973). By point E, the moisture has deepened considerably and is represented by schematic soundings 6b and 6c.

A schematic showing the vertical slice through a cell associated with "open cell" mesoscale cellular convection (Agee et al. 1973) is shown in the top portion of Fig. 7. This type of convection can best be seen at points D and E on the satellite imagery in Fig. 4. The schematic is a vertical cross section taken at those locations. The arrows in the schematic show convergence near the upper portion of the center of the cell, and subsiding motion as the arrows converge, resulting in a cloud-free center. However, there is convergence, rising motion, and cloud development on the periphery of each cell. This results in the area of many polygonal-shaped rings of convection with essentially clear centers seen near D and E.

On the other hand, at F there is closed cell development, and is seen in the bottom half of Fig. 7. The arrows indicate that the flow in a closed cell is opposite of that of an open

cell, with rising motion and cloud development in the center of the cell. There is sinking motion at the periphery of the cell, resulting in clear walls on the periphery of each cell. This cloud type can be seen at F in Fig. 4. Krueger and Fritz (1961) noted these two types of polygonal shaped cells. They identified the open cells as clear centers, about 15 to 25 km wide, surrounded by a wall of cumuliform clouds. The closed cells were identified as cloudy air, about 50 to 80 km wide, surrounded by walls of clear air. The convection is often only 1-2 km deep, for instance, at point D, but can be much deeper, for instance, at point E. Open cells can also be a good indicator of wind speed and direction (Pearson and Stogaitis 1988). Figure 8 shows how the cells can be distorted, or the ring of convection can be broken up in stronger winds. The diameter of the open cells is related more to the depth of instability than the wind speed (Pearson and Stogaitis 1988). The diameter usually increases downstream as the depth of the boundary layer increases due to convection, until a maximum depth of instability is achieved. This can be seen in the Fig. 9 schematic as well as in Fig 4. as the flow progresses from C to E.

A schematic showing roll-type convection which produces cloud streets is shown in Fig. 10. Also, from Staudenmaier (1995), Fig. 11 shows a schematic of roll-type convection (a slice taken perpendicular to the roll axis) and includes a typical sounding. Cloud streets are normally found in an unstable layer of air 1-3 km thick where the wind direction changes little with height. Frequently there is a capping temperature inversion. The streets form approximately along the direction of the wind , spaced about 2 to 8 km apart, and become wider as the convection deepens. With the deeper clouds, precipitation is possible. [The detailed theory behind the formation of roll-type and mesoscale cellular convection can be further obtained from Agee et al. (1973)].

A good example of convection over a large body of water can be seen in Andersson and Gustafsson (1994). They studied convective snowbands over the Baltic Sea on 11 January 1987 (Fig. 12) during a case of cold easterly flow. The satellite picture shows that the bands do not develop until the easterly flow destabilizes enough for convection to occur, so the band development may not begin until the air parcels move well out over the open water. Andersson and Nilsson (1990) noticed that leeward of large islands there is a characteristic cloud-free area. Near the middle of Fig.12 there is an island with a cloud free area behind the island.

The "cloud-free area downwind of the islands is one of the characteristics of many IE patterns, which will be illustrated later. An interesting feature associated with most of the southern California cases is that IE bands generated by the islands appear to be enhanced in comparison to other bands which may be present. During some conditions only one band is visible downwind from the island. Frequently an enhanced band will form around both sides of the island, and when combined with the cloud free zone, the result is a sort of "train track" pattern. This enhancement will be apparent for many of the IE cases that will be presented.

Lake-effect Rain Events

Miner and Fritsch (1997) studied seven years of lake-effect precipitation events downwind of Lake Erie. They constructed mean atmospheric environments for rain events and compared them to conditions for lake-effect snow events. They noted that the mean atmospheric conditions for rain events were similar to those found during lake-effect snow events. In particular, they found the following conditions were associated with lake-effect rain events;

1. Cold, post-frontal low-level flow
2. A nearly moist adiabatic layer below about 850 mb.
3. Wind increasing steadily with height
4. Minimal directional shear throughout the troposphere.

Composite soundings were made for the lake-effect rain conditions (Figs. 13 and 14). There is a striking resemblance between the lake-effect composite soundings and the soundings associated with IE case studies in the southern California Bight Region below.

Case Studies of Events in Southern California

CASE A. Island Effect on 15 April 1998

On 15 April 1998, lines of cumulus developed over the southern California Bight Region (Fig.15). (Locations mentioned are found on Fig. 1). The 1200 UTC 15 April 1998 KNKX raob (Fig. 16) showed a conditionally unstable, nearly saturated airmass over NKX at the lower levels. The flow was post-frontal, with a light northwest wind at the surface. The flow was unidirectional and steadily increasing with height for unidirectional shear. Mesoscale cellular convection was occurring over the outer waters. Enhanced lines of convection can be seen streaming southeast of Santa Catalina (AVX) and San Clemente (NUC) Islands, extending inland to the coastal slopes of the mountains. The lines appeared to have formed overnight, and a cloud-free region has developed downstream of Santa Catalina Island. The highest elevations on the islands are approximately 2000 feet. It appears that this is a formidable enough barrier to disturb the flow traveling past the islands, creating enhanced lines of convection in the cumulus field. The island wake and the strength of the bands downwind of Santa Catalina Island were stronger than those downwind of San Clemente Island. These IE bands resulted in enhanced showers as seen on the 1646 UTC 15 April 1998 KNKX composite reflectivity (Fig. 17). Within this IE banding in the San Diego area, small hail was reported at 1720 UTC. The 1800 UTC 15 April 1998 satellite imagery appears to show only a single main band extending southeast of both islands (Fig. 18), which illustrates the fact that the number of enhanced lines can vary, even during the same weather event.

CASE B. Island Effect on 8-9 November 1998

On 8 November 1998, a cold front moved through southern California. The 1200 UTC 9 November 1998 raob in Fig. 19a showed a conditionally unstable, nearly saturated airmass over KNKX up to about 780 mb. The flow was post-frontal, with a light northwest wind at the surface. The flow was unidirectional and steadily increasing with height for unidirectional shear. During this period convection was initiated. A line of showers developed east of Santa Catalina Island just south of Santa Ana (SNA). One-half inch of rain fell in 25 minutes along with small hail near SNA at 0805 UTC on 9 November 1998. The band (along with another band of convection generated by San Clemente Island) can be seen on the 0605 UTC 9 November 1998 KNKX composite reflectivity in Fig. 19b. The KNKX VAD wind profile at 0401 UTC 9 November 1998 and 1428 UTC 9 November 1998 showed a windshift from west to northwest overnight (not shown). The bands shifted south overnight, which is expected with a windshift from westerly to northwesterly. The 1530 UTC 9 November 1998 satellite imagery (Fig. 20) reveals a cloud-free zone downwind of San Clemente Island with bands on either side of the island. (Two of the large lines of convection over the SAN area were likely due to dissipating bands generated by Santa Catalina Island).

CASE C. Island Effect on 17 February 1998

On 17 February 1998, between 0600 UTC and 1800 UTC, a strong cold front with heavy rain moved through southern California. San Diego received over 1.5 inches of rain. The 2015 UTC 17 February 1998 visible picture shows IE bands generated by Santa Catalina and San Clemente Islands (Fig. 21). Further offshore is active open cell convection, with a few cells taking on the classic hexagonal pattern. Christian and Wakimoto (1989) noted that there were radar reflectivity maxima, spaced 3.0 to 8.0 km apart along the horizontal convective roll clouds in their study. The IE bands in this 17 February 1998 case have taken on this "pearls on a string" look (and this feature also appears in later cases). At 0000 UTC 18 February 1998 (Fig. 22), the NKX raob was still unstable, with a lifted index of -1. The airmass was still moist below about 6000 feet, but was drying rapidly aloft. The flow was typical post-frontal flow, unidirectional and increasing steadily with height. There was no strong stable layer evident on the raob. At 0113 UTC 18 February 1998, the three main convective lines were still clearly visible on the radar with weaker lines also visible (not shown). The Santa Catalina Island IE band still maintained the "pearls on a string" look, with some cells as strong as 50 dBZ (Fig. 23a). At 0203 UTC 18 February 1998, the radar showed four distinct bands, likely generated by the flow past the islands (Fig. 23b). The lines persisted well into the evening. At 0541 UTC 18 February 1998, small hail was reported north of San Diego.

CASE D. Island Effect on 25 February 1998

On 25 February 1998 at 0030 UTC, IE bands developed downwind of Santa Catalina and San Clemente Islands in Fig. 24. There was very active open cell convection west and south of the bight. There were about four major bands. There were lesser bands between them, most likely due to the development of horizontal roll convection. The 0000 UTC 25 February 1998 NKX raob (Fig. 25) showed a conditionally unstable, nearly saturated airmass over KNKX up to about 750 mb. The flow was post-frontal, with a light northwest wind at the surface. The flow was unidirectional and steadily increasing with height for unidirectional shear, which seems to be common during these events. The 0031 UTC 25 February 1998 KNKX composite reflectivity showed the locations of the main bands of convection (Fig. 26).

CASE E. Island Effect on 7 April 1998

On 7 April 1998 at 2330 UTC, IE bands were visible downwind of Santa Catalina and San Clemente Islands in Fig. 27. There was very active open cell convection west and south of the bight, and cloud streets developing over the coastal areas. The 0000 UTC 7 April 1998 raob showed a well-mixed airmass at the lower levels (Fig. 28). The flow was post-frontal, with a light northwest wind at the surface. The flow was unidirectional and steadily increasing with height for unidirectional shear. The band showed "pearls on a string" characteristics, similar to those seen on the roll clouds that have developed over the coastal areas . This may indicate that the same instability that develops in roll clouds also develop in IE bands. This is similar to the observations in Riehl (1954). Riehl wrote "On days with east-southeast to southeast winds a cloud street extended downstream from an isolated mountain on the eastern end of Puerto Rico. When the cloud street was fully developed, it consolidated into a single imposing roll cloud. The length of the cloud was 20 to 40 miles, its lateral width barely a mile. It extended from 2000 to 8000-10000 feet altitude. The cloud organizes shortly before noon and dissipates 3-4 hours later, shifting its position very little. In that time more than 4-5 inches of rain may fall in the narrow underlying zone. The size of the raindrops was huge, larger than any that the author (Riehl) had seen falling from cumulonimbus. The top of the roll cloud was not uniform. Peaks and valleys alternate, with amplitude of 1000-2000 feet and spacing of a few miles, indicating superposition on the roll a wave motion". This does seem to parallel some of the aspects that occur with some IE bands. Notice the huge field of well-formed open cell over the outer coastal waters, very weak streets over the inner coastal waters, and well-developed streets over the land.

CASE F. Island Effect on 9 February 1998

The 2030 UTC 9 February 1998 visible satellite imagery (Fig. 29) showed a band downwind of San Clemente Island and another downwind of San Nicolas Island. The 1200 UTC NKX raob in Fig. 30 showed a post-frontal airmass, which was nearly saturated up to 800 mb and conditionally unstable. The flow was unidirectional, and increased steadily

with height. Horizontal roll convection had developed over the land as well as over the waters of the bight near San Clemente Island.

CASE G. Island Effect on 30 October 1998

Two bands of convection enhanced by Santa Catalina Island developed during the morning hours on 30 October 1998. Rain developed between 0900 and 1000 UTC 30 October 1998 and increased in intensity as the band shifted south. In the San Diego area, Chula Vista picked up 0.71 inches of rain between 1200 and 1300 UTC shown in Fig. 31. When the band moved south, Lower Otay Reservoir picked up 0.87 inches between 1300 and 1400 UTC shown in Fig. 32. The 1200 UTC 30 October 1998 NKX raob in Fig. 33 showed a conditionally unstable, nearly saturated airmass over NKX at the lower levels. The flow was post-frontal, with a light wind at the surface. The flow was generally unidirectional and steadily increasing with height for unidirectional shear. The 1300 UTC 30 October 1998 NKX infrared satellite imagery in Fig. 34 shows a band of heavy rain in the Chula Vista and Otay Reservoir area. The 1343 UTC 30 October 1998 KNKX STP showed the band extending southeast from Santa Catalina Island in Fig. 35. The 1600 UTC 30 October 1998 visible satellite imagery in Fig. 36 shows the bands colliding, which may help to explain the heavy rain earlier.

CASE H. Island Effect on 4-5 December 1998

Early in the morning of 4 December 1998 and again on 5 December 1998, IE bands formed over the coastal waters. On the morning of 4 December 1998, a "train track" type cloud pattern developed over the coastal waters downwind from the islands in the moist airmass behind the first cold frontal passage. The bands can be seen on the 1730 UTC 4 December 1998 satellite imagery in Fig. 37. By afternoon, another cold front swept through the area, leaving the region under westerly flow, that veered to north-northwesterly flow overnight and into the following morning. This shift in the wind can be seen in the Redondo Beach buoy observations shown in table 1. By 0000 UTC 5 December 1998, as the cold, moist, and unstable airmass began to settle over the area, two main bands, a result of the low-level flow around Santa Catalina Island, developed northeast of the island. Evidence of the bands can be seen on the 0657 UTC 5 December 1998 KSOX Storm Total Precip and in the 1818 UTC 5 December 1998 KSOX Storm Total Precip in Figs. 38 and 39 respectively. At 0730 UTC 5 December 1998 a spotter reported "penny" sized hail in the area. As the winds shifted to a more northerly direction, the IE bands moved southward. The 1724 UTC 5 December 1998 KNKX storm total precip in Fig. 40 showed the evening position of the Santa Catalina Island IE bands just south of SNA and the late night position of the IE bands about five miles southwest of the KNKX RDA. IE bands, which appear to be the result of San Clemente Island can be seen about 25 miles southwest of the RDA. The bands resemble "train tracks". The bands streaming downstream from the Islands can also be seen on the 1600 UTC 5 December 1998 visible satellite imagery in Fig. 41. As in many other IE cases, the 1200 UTC 5 December 1998 NKX raob in Fig. 42 indicated a nearly saturated, conditionally unstable airmass at the lower levels. The winds increased steadily with height and there was unidirectional shear.

CASE I. Island Effect on 25-26 January 1999

During the late morning hours on 25 January 1999, IE bands developed off San Nicolas Island (NSI) and extended east toward the area between SNA and CRQ. These convective enhancements in the flow can easily be seen in Fig. 43. The airmass was conditionally unstable in the lowest layers on the 1200 UTC 25 January 1999 NKX raob (Fig. 44). The 0000 UTC 26 January 1999 raob (Fig. 45) indicated that the conditionally unstable layer continued to deepen during the day, and showed the common profile for the development of IE bands. The 0000 UTC 26 January 1999 raob also indicated that the flow was post-frontal, with a light wind at the surface. The flow was generally unidirectional and steadily increasing with height for unidirectional shear. The 1800 UTC 25 January 1999 surface plot (Fig. 46.) showed northwest flow around VBG that became more westerly over the coastal waters, where the flow moved over San Nicolas Island.

CASE J. Island Effect on 26 February 1996

26 February 1996 was the first documentation of the IE on the newly-installed Miramar (KNKX) WSR-88D Radar. The 1200 UTC 26 February 1996 raob showed a conditionally unstable airmass over NKX at the lower levels (Fig. 47). The flow was post-frontal, with a light wind at the surface, remaining unidirectional, and steadily increasing with height for unidirectional shear. (The frontal passage occurred about *24 hours* earlier.) This wind, moisture, and instability pattern hints at the possibility of IE bands. The 2046 UTC 26 February 1996 NKX radar showed an IE band intersecting the coast between SNA and CRQ in Fig. 48. Cells of about 40 dBZ were over the area. The line was quasi-stationary, with mainly light to moderate showers. The apparent instability of the airmass is also supported by the hexagonal open cell convection just south of the California/Mexican border. The 2046 UTC 26 February 1996 NKX WSR-88D VAD wind profile (not shown) showed a wind profile similar to the 1200 UTC 26 February 1996 raob, so the winds had changed little; unidirectional, and steadily increasing with height for unidirectional shear. This profile also supports the observation of the IE band and open-cell convection.

Discussion and Conclusion

From the above examples, it can be seen that there is a distinct set of conditions under which IE bands generally develop. The forecaster can look for;

1. Cold, post-frontal onshore low-level flow.
2. A conditionally unstable or moist adiabatic airmass at the lower levels.
3. Wind speed increasing steadily with height.
4. Unidirectional shear.

It has been seen that IE bands can form in post-frontal environments under conditions very similar to those found during Lake Effect events. The conditions parallel those seen during the occurrence of open/closed cell convection and cloud streets. Frequently they form in the vicinity of the IE bands. The appearance of open/closed cell convection and cloud streets behind a cold front should alert the forecaster to the possibility of IE band development.

A thorough knowledge of the conditions that result in IE bands is very important. This is because frequently when the main area of upward forcing exits the region and downward motion develops over the region, IE bands can still activate and produce additional showers and thunderstorms. This can occur even when areas away from the bands are clearing. It is also seen that although many of the studies on lake-effect phenomena are in relation to snowstorms, it can also be easily extended to cases without snowfall being the main concern, which is certainly the case here. Boating and aviation, as well as driving conditions can be adversely affected by IE phenomena as visibilities can drop rapidly in showers and thunderstorms. IE bands, as well as open cells and cloud streets, can be prolific small hail producers, especially when the freezing level falls below about 6000 feet. The spotter report of "penny-sized hail" in the 4-5 December 1998 case indicates that there is also a problem of severe thunderstorms to consider.

There is another reason why these phenomena should not be taken lightly. On 15 April 1998, on IE bands generated by Santa Catalina Island, two funnel clouds were spawned almost simultaneously, one on the band near SAN and another on the band near CRQ. The bands associated with the funnel clouds were shown in Fig. 17. This topic will be discussed in future research.

It should be pointed out that there are other mechanisms that result in the development of persistent bands of showers and thunderstorms over the coastal waters. In Fig. 43 on 25 January 1999, there is a line of thunderstorms stretching from near VBG southeast to near AVX. There is also an east-west line of thunderstorms west of SAN. These lines are likely to be generated by the dynamics of the vorticity center that moved directly over the area. (The presence of a vorticity center over the Bight Region is an excellent example of a prolific hail pattern).

Finally, looking back to Fig. 20, the cloud band enhanced by flow past San Clemente Island appears to begin about 30 miles *before* reaching San Clemente Island, then splits downwind of the island. This suggests that there is another terrain-related mechanism that has helped with the development of the bands. A mesoscale convergence zone develops. This convergence zone consists of airflow from the Pacific toward the coast, converging with one or more of the following:

1. A relatively cold nocturnal boundary layer that can evolve into a land breeze front.
2. Terrain-forced flow along the mountains (blocking/barrier jet).
3. Downslope flow west of the mountains.

This convergence zone has been seen to develop in the past under certain conditions (mainly during post-frontal patterns) and is currently under investigation.

Acknowledgments

I would like to thank Armando Garza and Ed Clark for their review, comments, and invaluable suggestions for this TA. I also wish to thank Greg Martin for graphical assistance.

References

Agee, E. M., Chen, T. S. and K. E. Dowell, 1973: A Review of Mesoscale Cellular Convection., *Bull. Amer. Meteor. Soc.*, **54**: 1004-1012.

Agee, E. M. and M. L. Hart, 1990: Boundary Layer and Mesoscale Structure over Lake Michigan During a Wintertime Cold Air Outbreak. *J. Atmos. Sci.*, **47**: 2293-2316.

Agee, E. M. and S. R. Gilbert, 1989: An Aircraft Investigation of Mesoscale Convection over Lake Michigan during the 10 January 1984 Cold Air Outbreak. *J. Atmos. Sci.*, **46**: 1877-1897.

Andersson, T., and N. Gustafsson, 1994: Coast of Departure and Coast of Arrival: Two Important Concepts for the Formation and Structure of Convective Snowbands over Seas and Lakes. *Mon. Wea. Rev.,* **122**, 1036-1049.

Andersson, T., and S. Nilsson, 1990: Topographically Induced Convective Snowbands over the Baltic Sea and Their Precipitation Distribution. *Wea. Forecasting*, **5**, 299-312.

Atkins, N. T. , R. M. Wakimoto, and T. M. Weckwerth., 1995: Observations of the Sea Breeze Front during CaPE. Part II: Dual-Doppler and Aircraft Analysis. *Mon Wea. Rev.,* **123**, 944-969

Bader, M..J. Bader, G. S. Forbes, J. R. Grant, R. B. E. Lilley, and A. J. Waters., 1995: *Images in Weather Forecasting*. Cambridge University Press, New York 499 pp.

Clark, J. H. and S. R. Dembek, 1990: The Catalina Eddy Event of July 1987: A Coastally Trapped Mesoscale Response to Synoptic Forcing. Mon. Wea. Rev., **119**, 1714-1735.

Doswell, C. A.., 1985: The Operational Meteorology of Convective Weather, Volume II: Storm Scale Analysis. NOAA Technical Memorandum ERL ESG-15. Environmental Sciences Group Boulder, Colorado. 240 pp.

Hales, J. E., Jr., 1985: Synoptic features associated with Los Angeles Tornado Occurrences. *Bull. Amer. Meteor. Soc.*, **66**, 657-662.

Hubert, L. F., 1966: Mesoscale Cellular Convection. Meteorological Satellite Laboratory Report No. 37, Washington D. C. , 68 pp.

Krueger, A. F., and S. Fritz, 1961: Cellular Cloud Patterns Revealed by TIROS I, *Tellus*, **13**, 1-7

LeMone, M. A.., 1973: The Structure and Dynamics of Horizontal Roll Vortices in the Planetary Boundary Layer. *J. Atmos. Sci.*, **30**, 1077-1091

Mass, C. F., and M. D. Albright, 1989: Origin of the Catalina Eddy. *Mon. Wea. Rev.*, **117**, 2406-2436.

Mass, C. F., and M. D. Albright, 1987: Coastal southerlies and alongshore surges of the west coast of North America; Evidence of mesoscale topographically trapped response to synoptic forcing. *Mon. Wea. Rev.*, **115**, 1707-1738.

Miner, T. J., and J. M. Fritsch, 1997: Lake-Effect Rain Events. *Mon. Wea. Rev.*, **125**, 3231-3248.

Riehl, H., 1954: *Tropical Meteorology*. McGraw Hill Book Company, Inc. New York 392 pp.

Staudenmaier, M., 1995: Convective Horizontal Roll Vortices As Viewed by WSR-88D. *Western Region Technical Attachment No. 95-16*, 4pp. National Weather Service Western Region, P. O. Box 11188, Salt Lake City, UT 84147.

Velarde, M. G., and C. Normand, 1980: Convection. *Sci. Amer.*, **243**, 92-109.

Wakimoto, R. M.., 1987: The Catalina Eddy and its Effect on Pollution Over Southern California. *Mon. Wea. Rev.*, **115**, 837-855.

*W*eckwerth, T. M., J. W. Wilson, R. M. Wakimoto, N. A. Crook, 1997: Horizontal Convective Rolls: Determining the Environmental Conditions Supporting their Existence and Characteristics. *Mon. Wea. Rev.*, **125**, 505-526.

Whitney, W. M., R. L. Doherty, B. R. Colman, 1993: A Methodology for Predicting the Puget Sound Convergence Zone and Its Associated Weather. *Wea. Forecasting*, **8**, 214-222.

file with
TA 99-18

AN OBSERVATIONAL STUDY OF ISLAND EFFECT BANDS: PRECIPITATION PRODUCERS IN SOUTHERN CALIFORNIA

Ivory J. Small
NWSO San Diego, CA
(Figures)

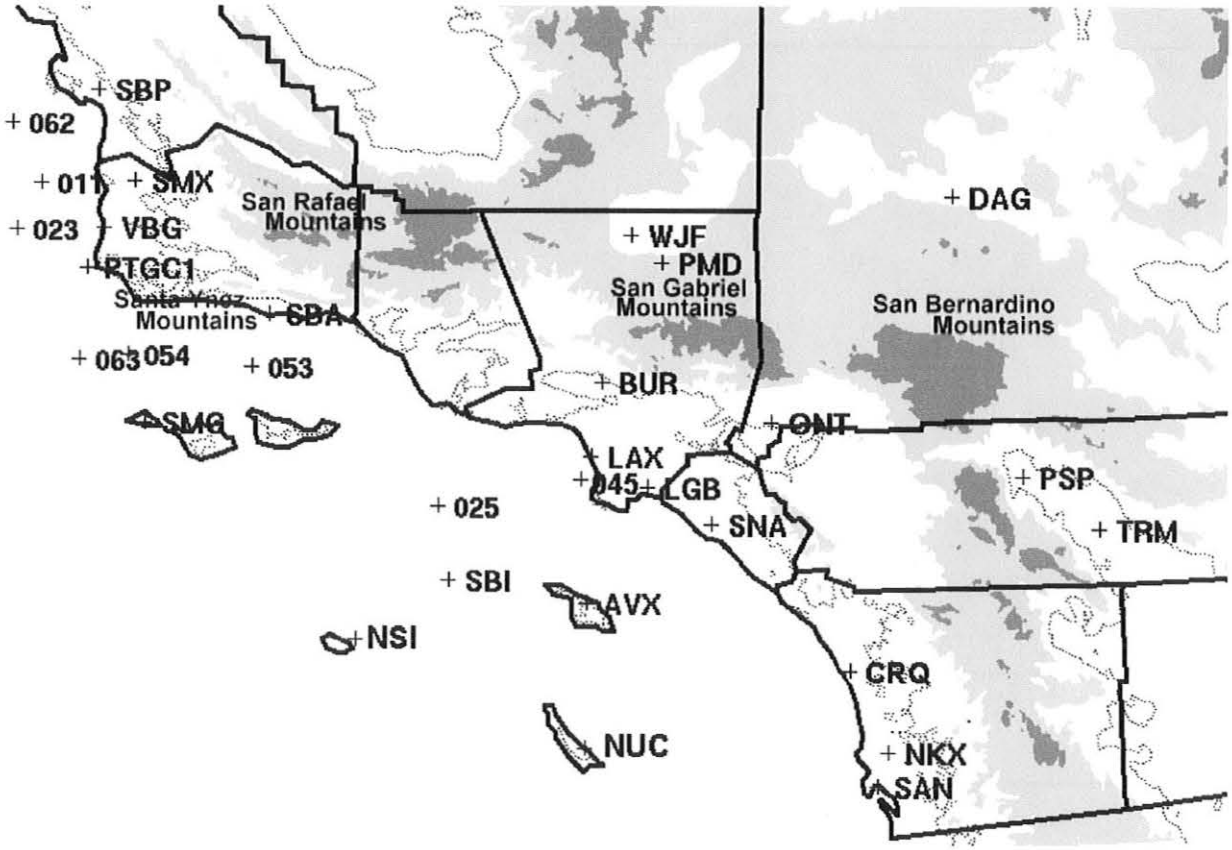

Fig. 1. Topographical features and geographical features in the Southern California Bight Region.

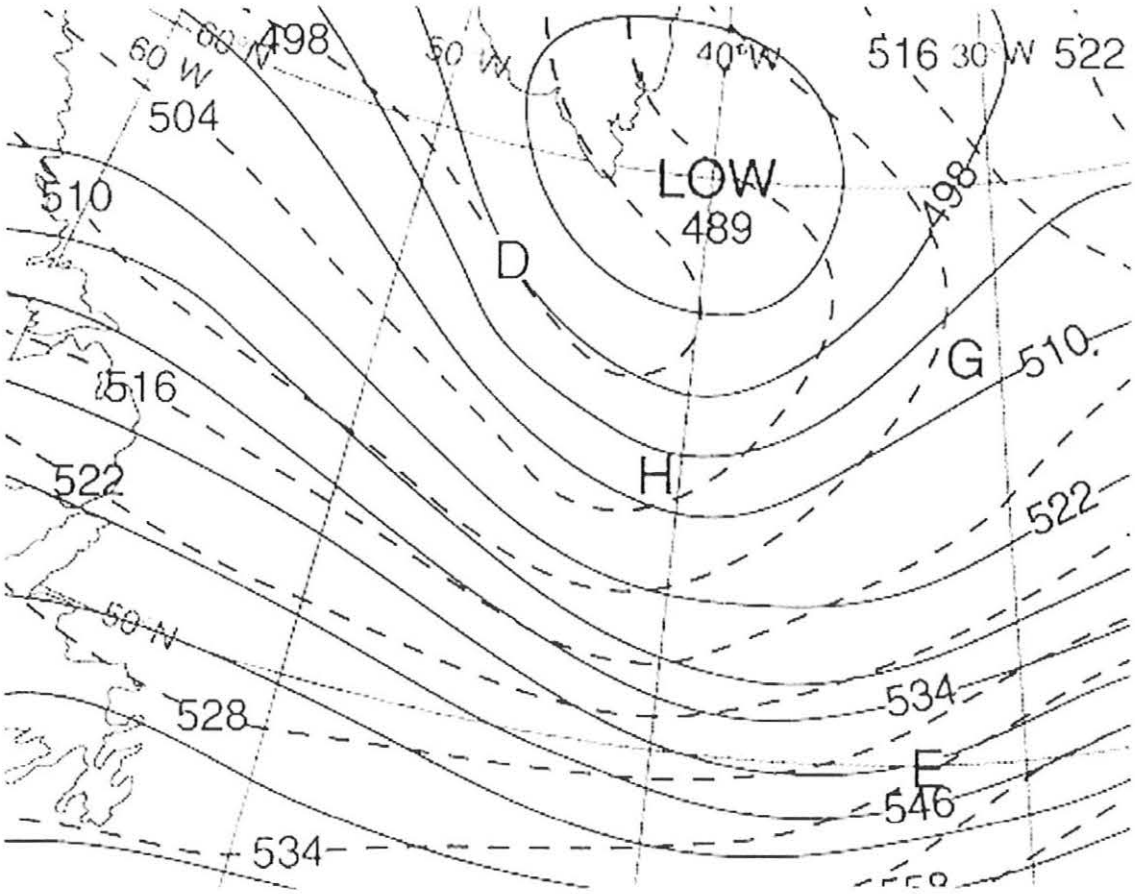

Fig. 2. 500 MB heights (solid) and 1000-500 MB thickness schematic for 1200 UTC 23 March 1986 (After Bader et al. 1995).

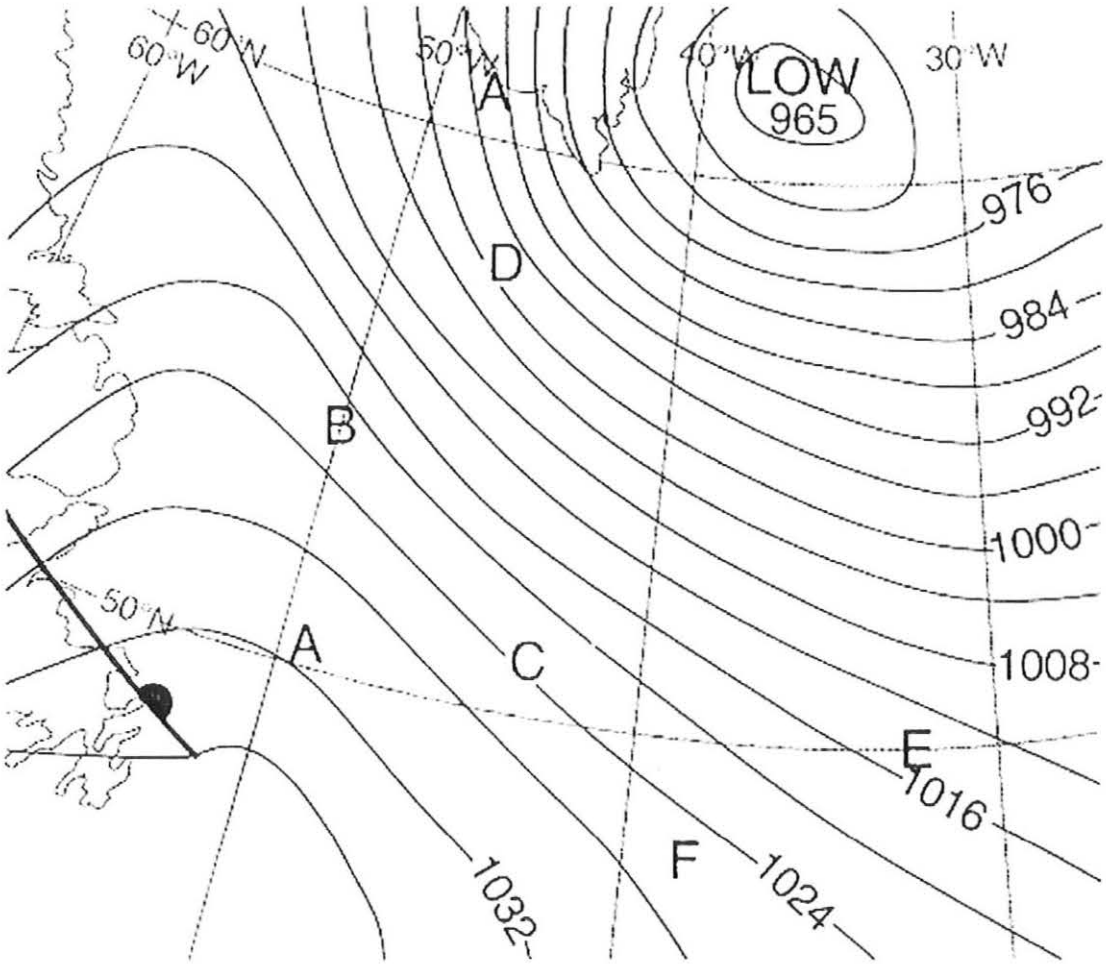

Fig. 3. Surface schematic for 1200 UTC 23 March 1986 (After Bader et al. 1995).

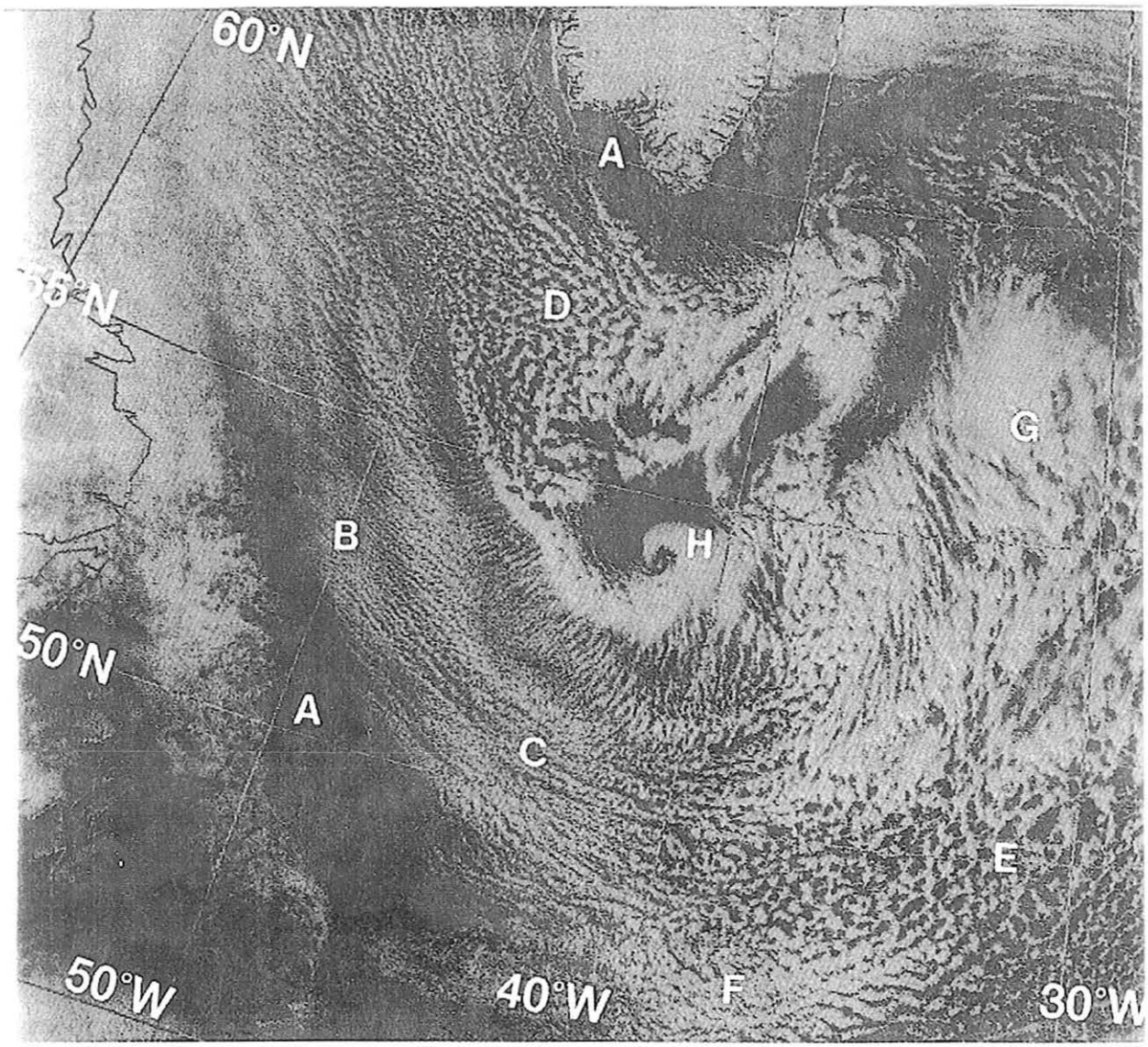

Fig. 4a. Visible satellite imagery for 1200 UTC 23 March 1986 (After Bader et al. 1995).

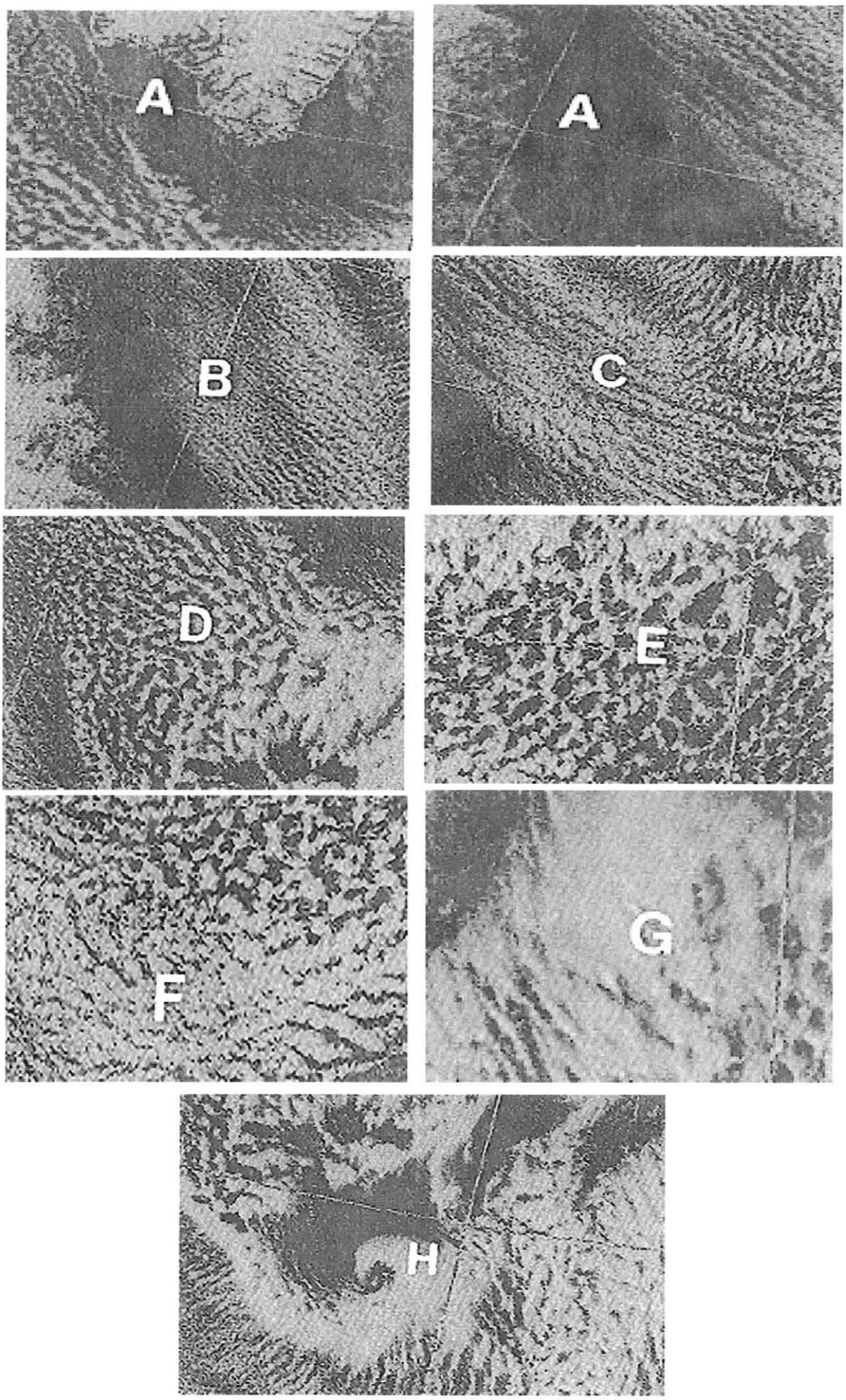

Fig. 4b. Visible satellite imagery over the North Atlantic for 1200 UTC 23 March 1986 showing locations A-H (After Bader et al. 1995).

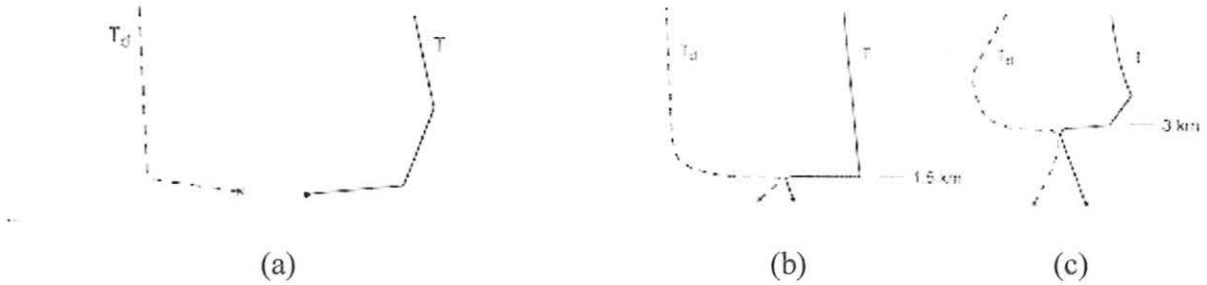

(a) (b) (c)

Fig. 5. Typical tephigrams associated with points A, B, and C on the 1200 UTC 23 March 1986 schematics and satellite imagery (After Bader et al. 1995).

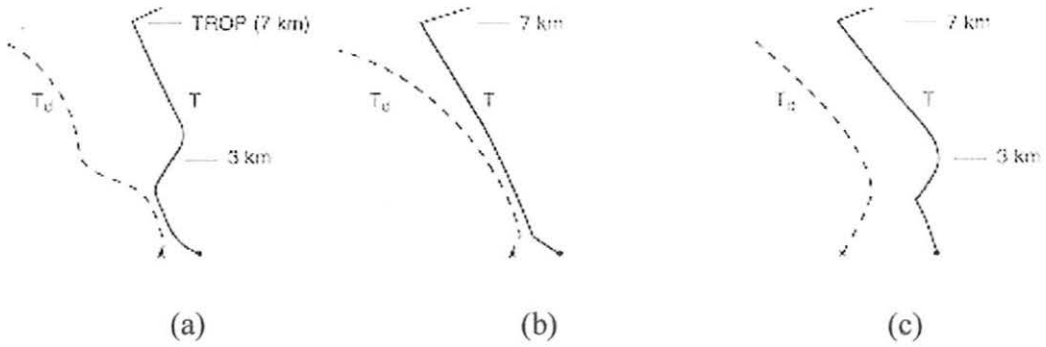

(a) (b) (c)

Fig. 6. Typical tephigrams associated with points D and E on the 1200 UTC 23 March 1986 schematics and satellite photo. The sounding at (a) represents the airmass near D, (b) represents the sounding in a Cb cloud in a deep open cell near E, and (c) represents the sounding in a cloud-free center of a deep open cell near E (After Bader et al. 1995).

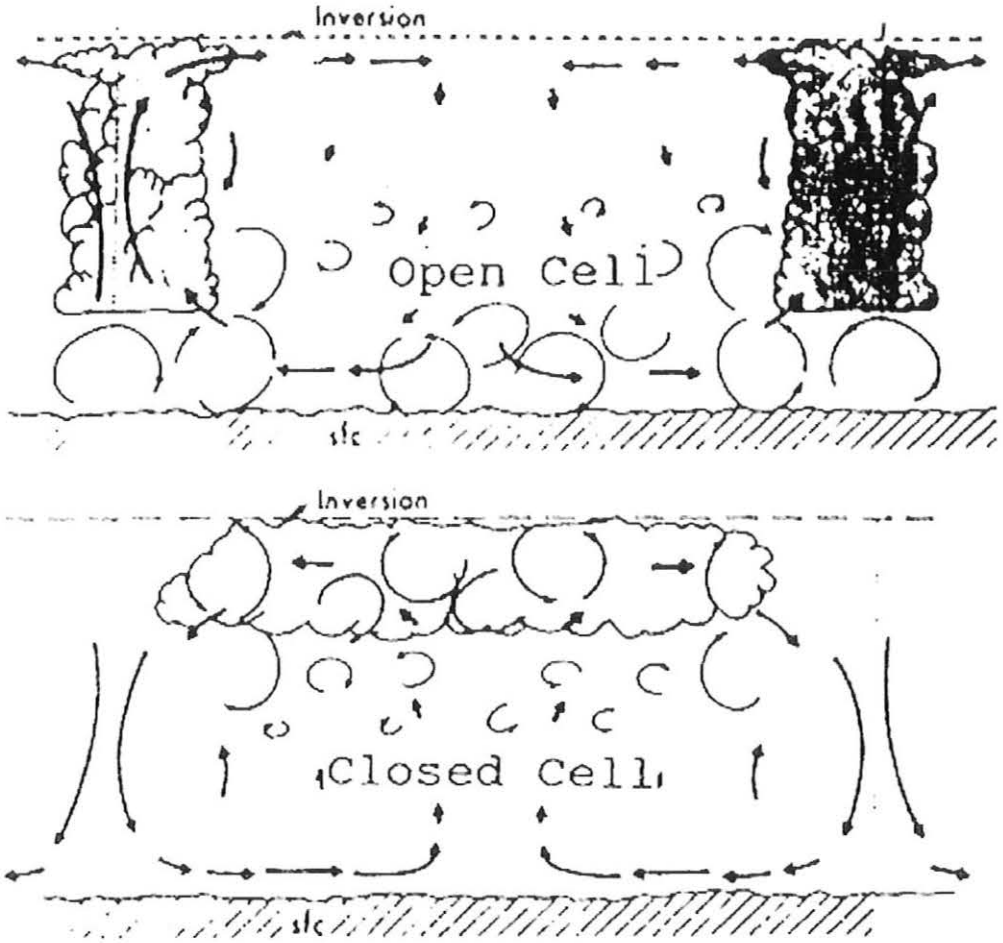

Fig. 7. Cross section of open (top) and closed (bottom) cell convection. The heavy arrows indicate mesoscale cellular circulation and the light arrows indicate turbulent motion (After Hubert 1966).

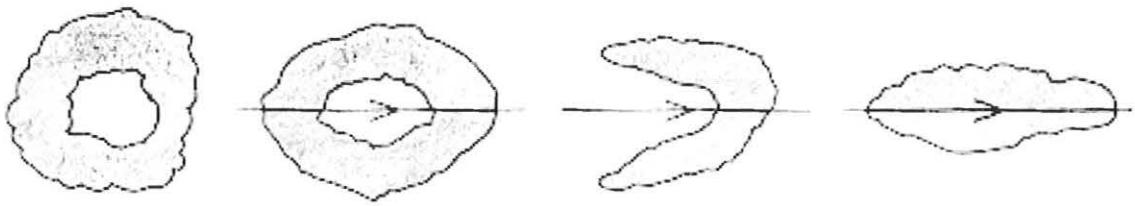

< 10 knots 11-20 knots 21-30 knots > 30 knots

Fig. 8. Changes in cell patterns with wind speed; the arrow shows the wind direction. (From Pearson and Stogaitis 1988).

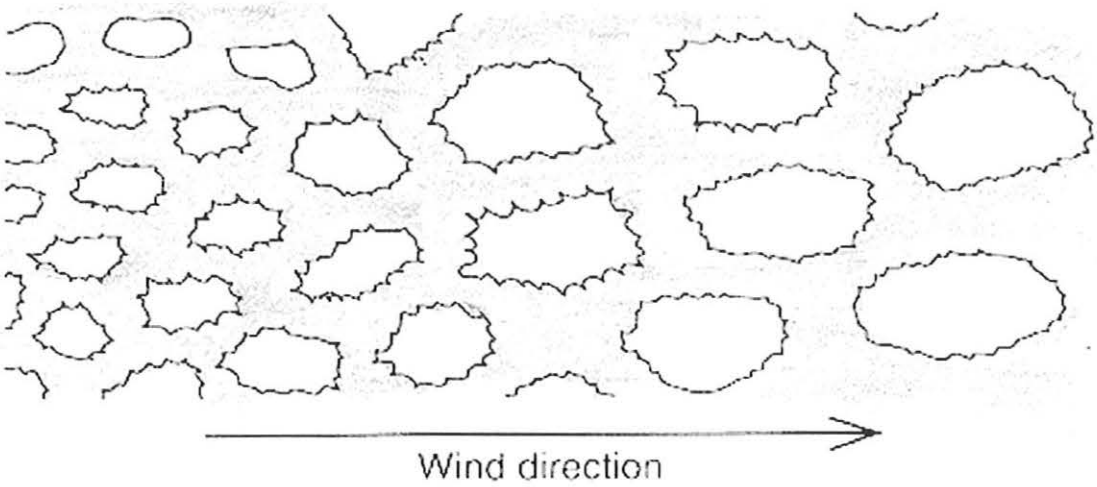

Fig. 9. Open cell diameter increasing with distance downstream; the cloud is shaded. (After Pearson and Stogaitis 1988).

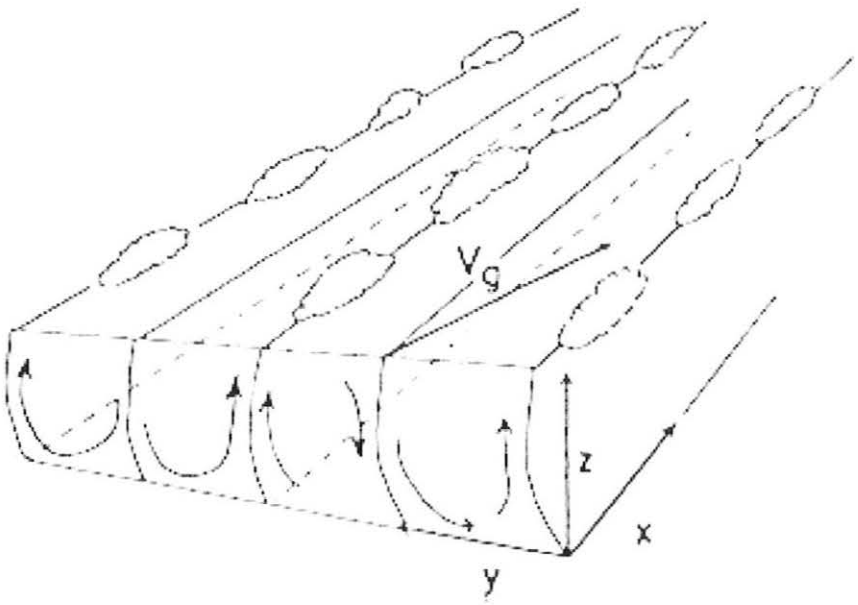

Fig. 10. Schematic showing roll-type convection which produces cloud streets. The vector V_g is the geostrophic wind vector (After LeMone 1973).

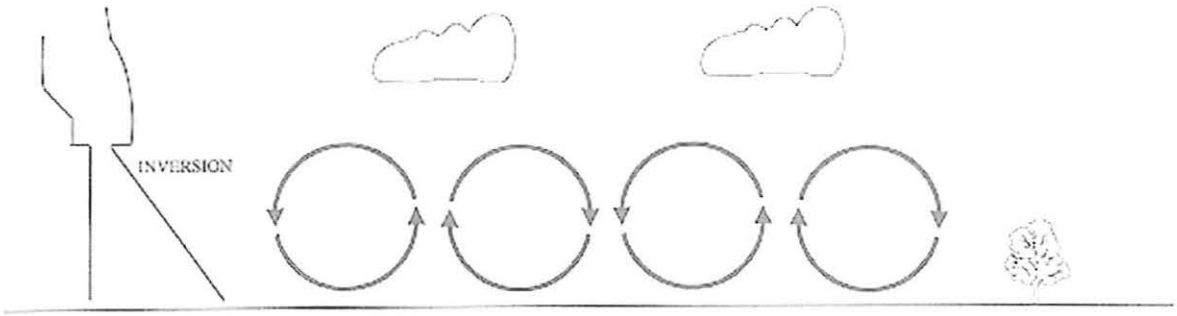

Fig. 11. Schematic vertical cross section perpendicular to two cloud streets showing the vertical circulation along with a sounding (After Staudenmaier 1995).

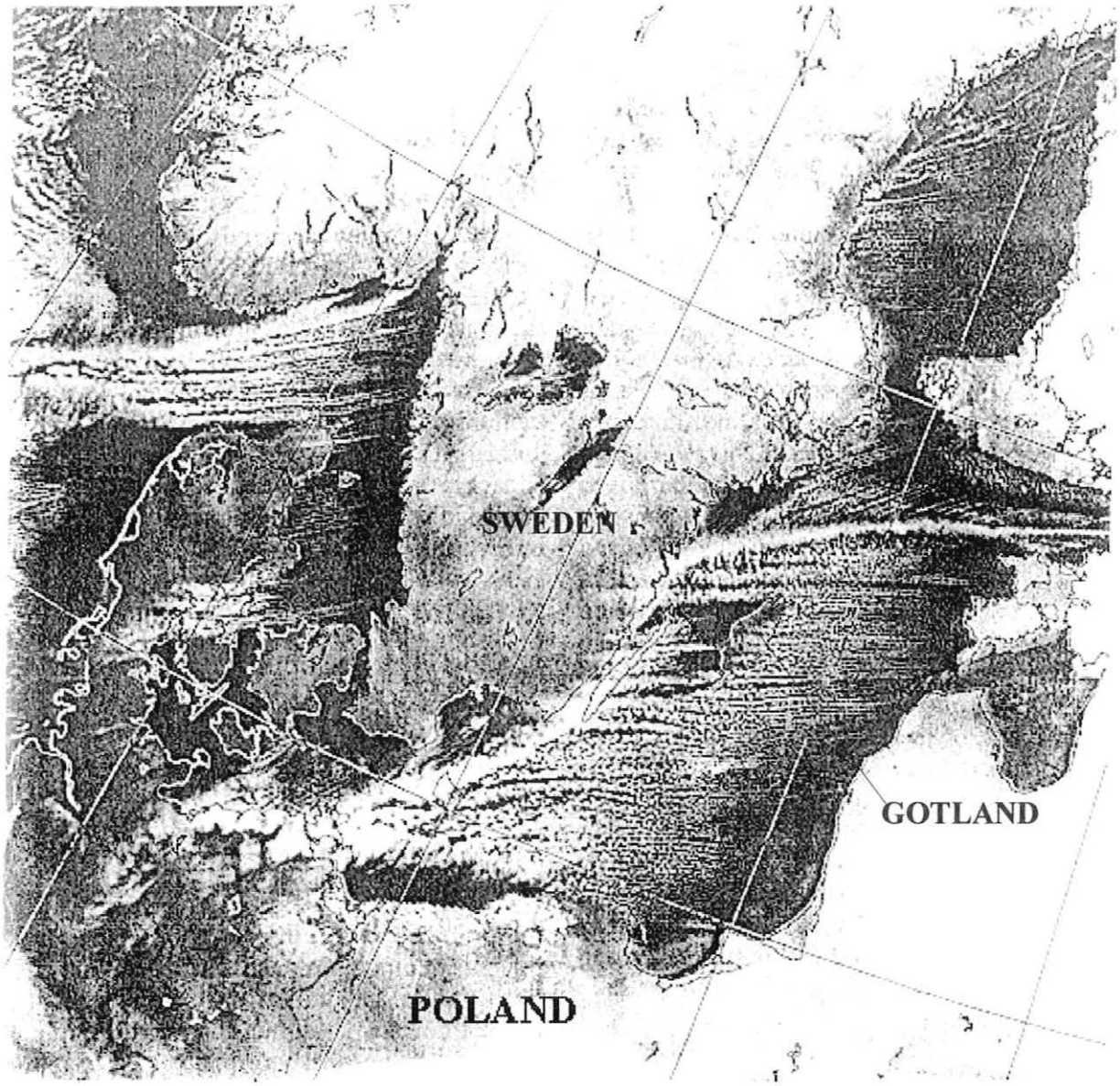

Fig. 12. Infrared satellite imagery at 1235 UTC 11 Jan 1987 showing snow bands over the seas (After Andersson and Gustafsson 1994).

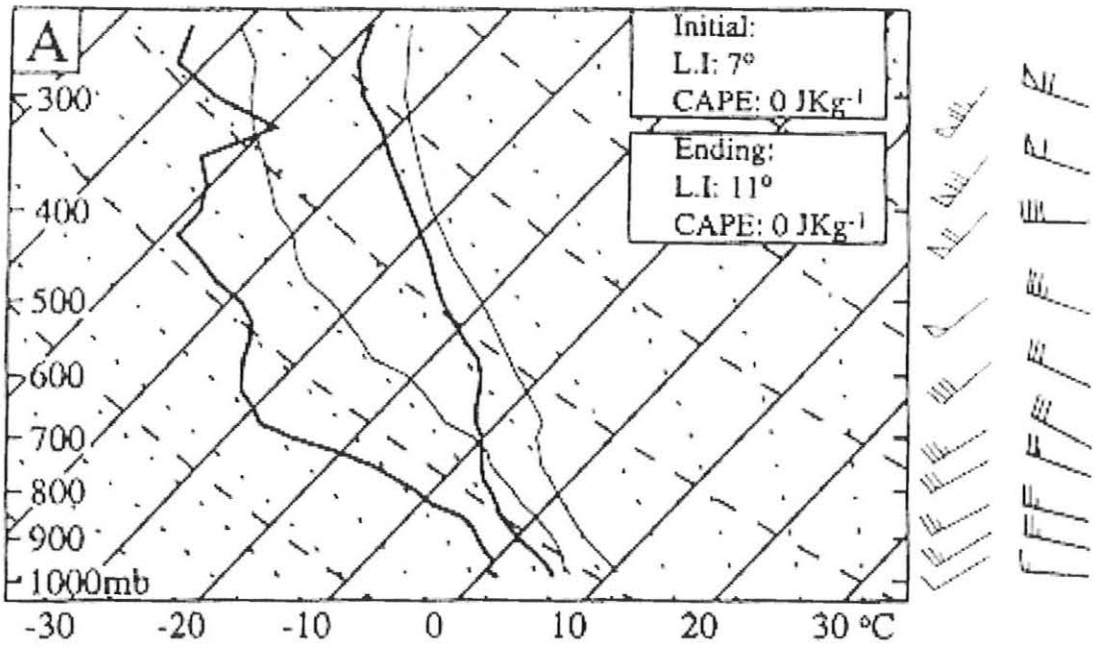

Fig.13. Mean Buffalo, New York soundings from the initial (thin lines) and ending stages (bold lines) of events (After Miner and Fritsch 1997).

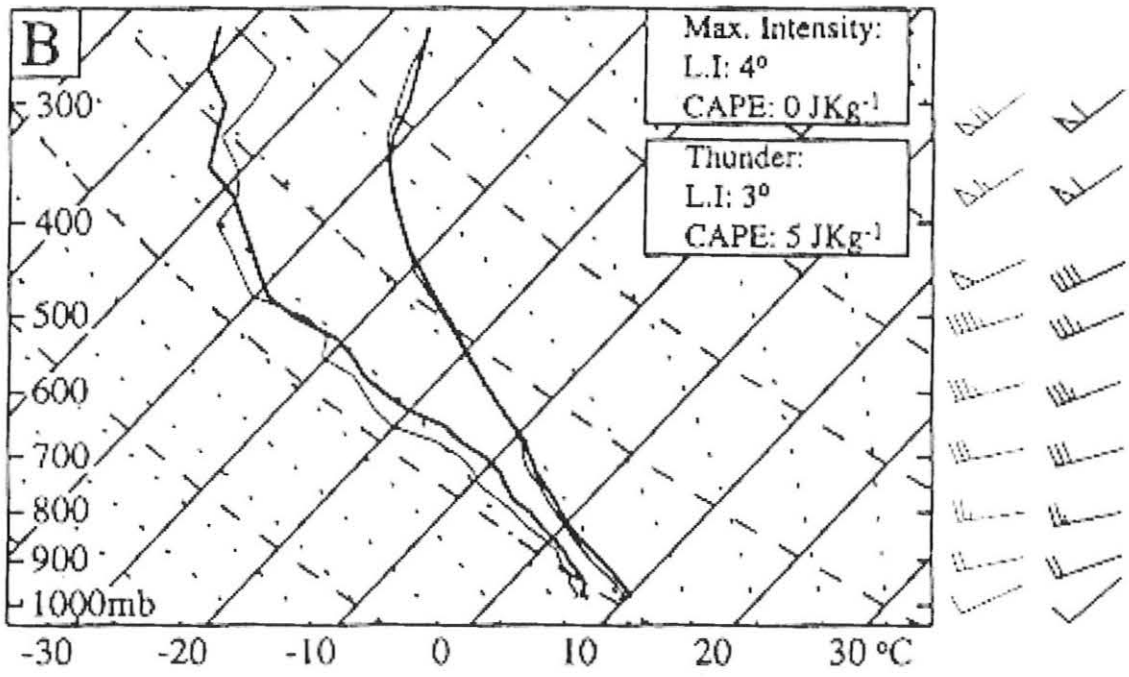

Fig.14. Mean Buffalo, New York soundings from the periods of maximum intensity (thin lines) and the periods containing thunder (bold lines) during events (After Miner and Fritsch 1997).

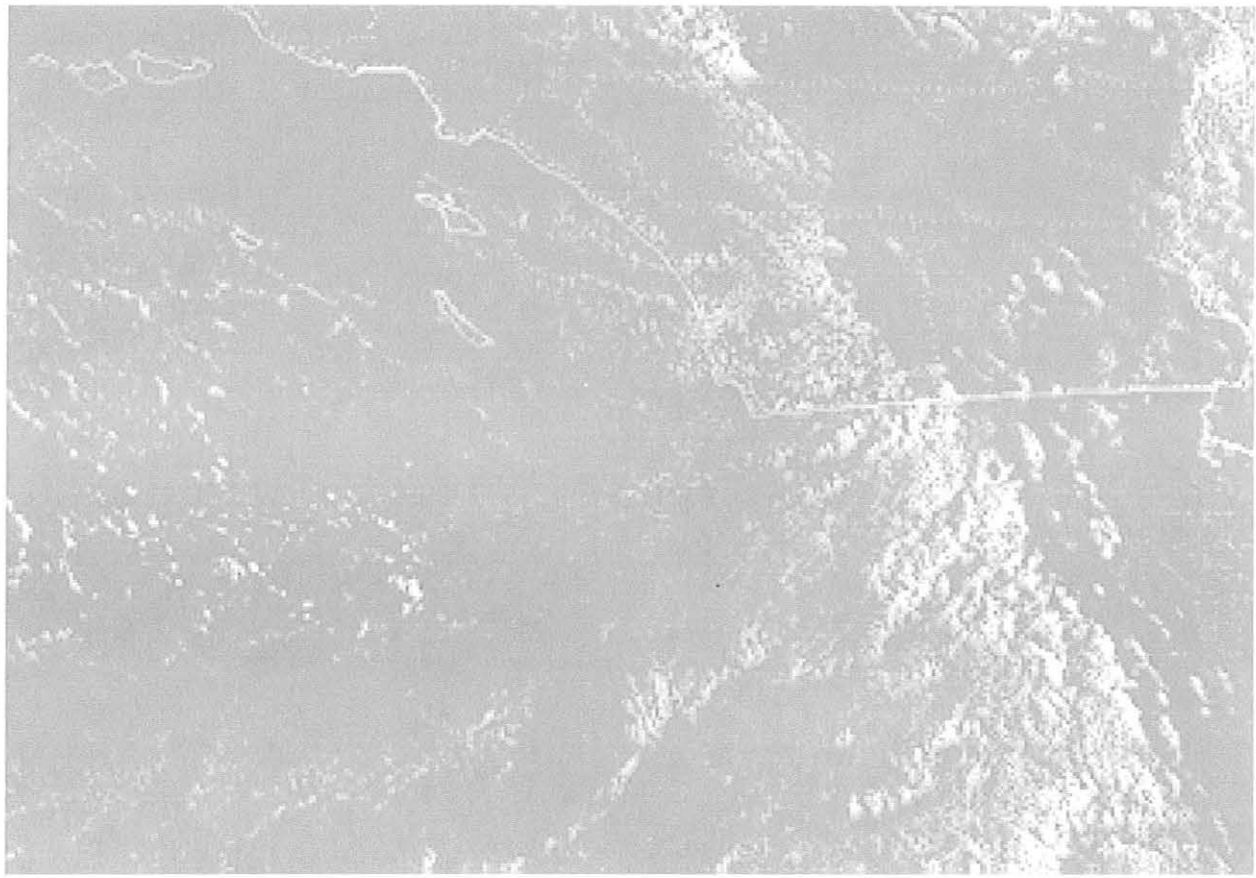

Fig. 15. 1500 UTC 15 April 1998 visible satellite imagery .

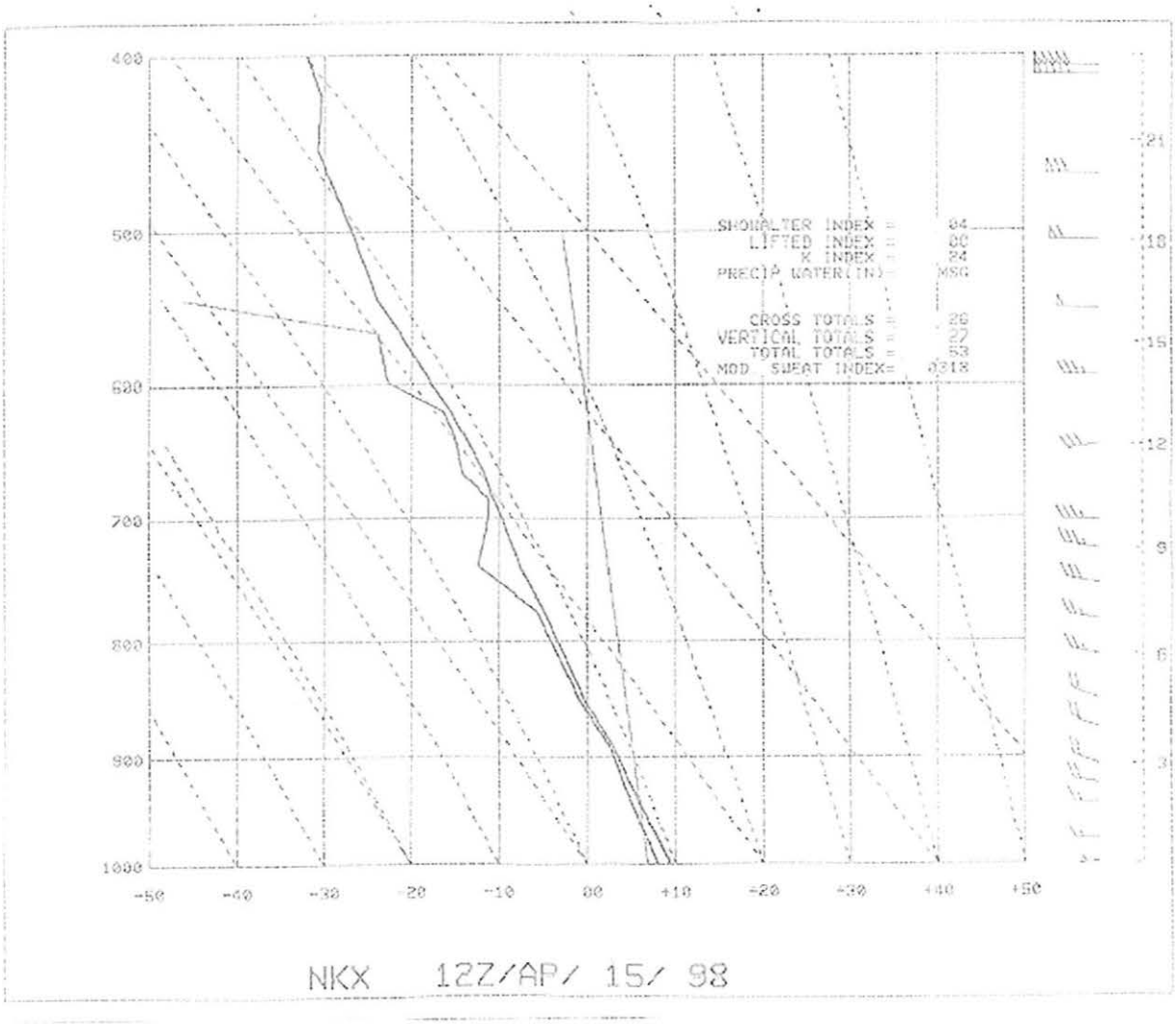

Fig. 16. 1200 UTC 15 April 1998 NKX sounding.

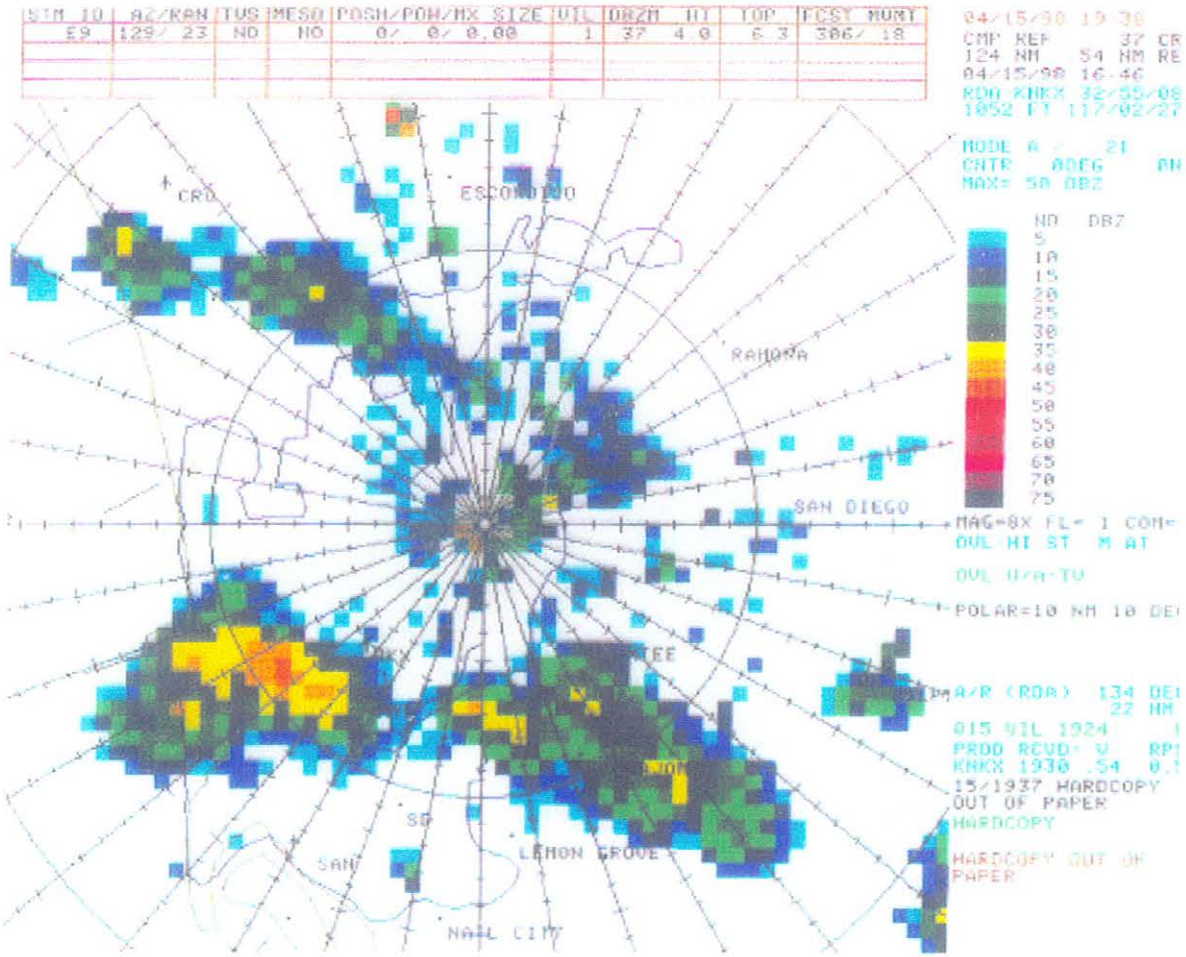

Fig. 17. 1646 UTC 15 April 1998 composite reflectivity from the KNKX radar.

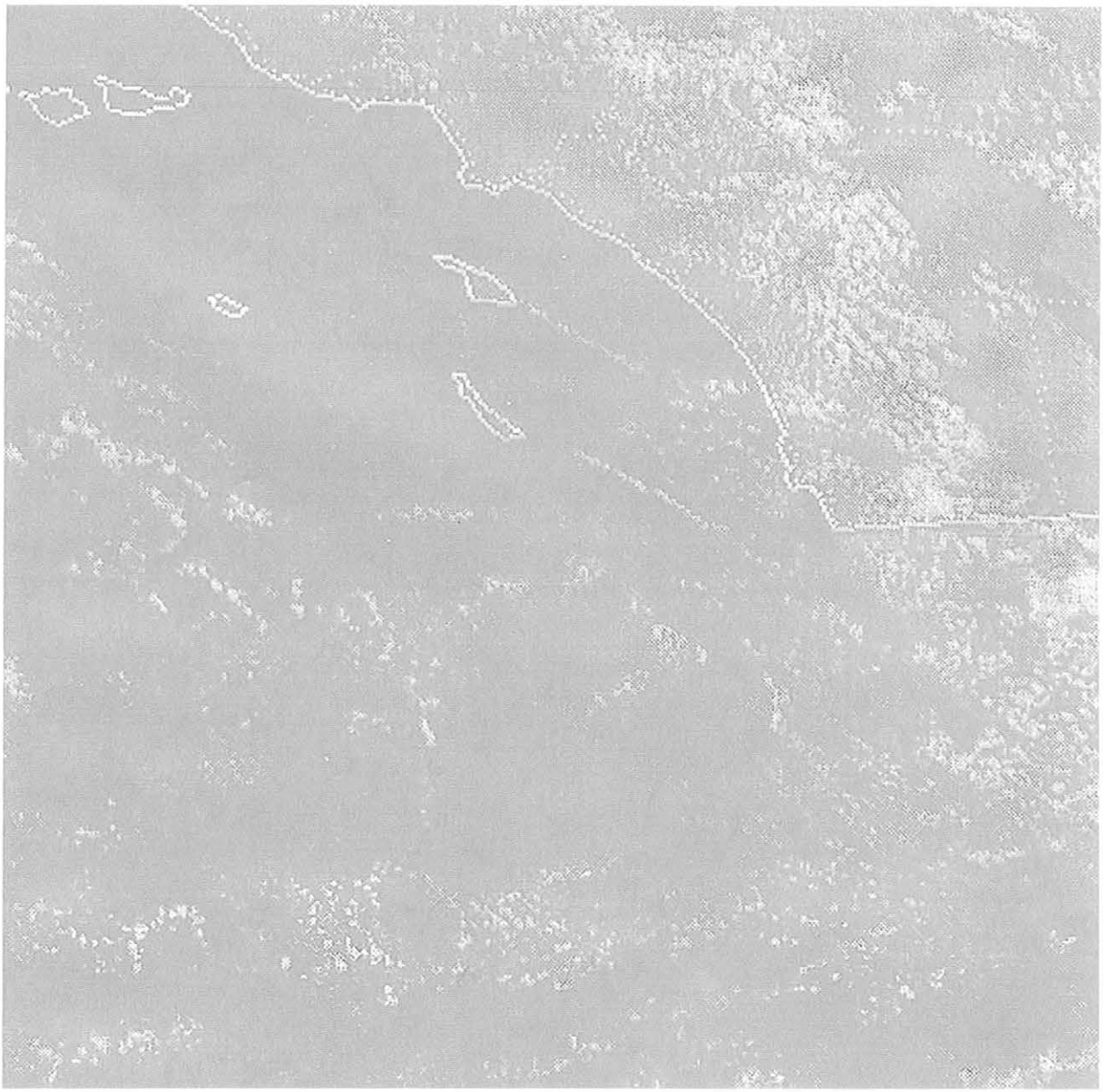

Fig. 18. 1800 UTC 15 April 1998 visible satellite imagery.

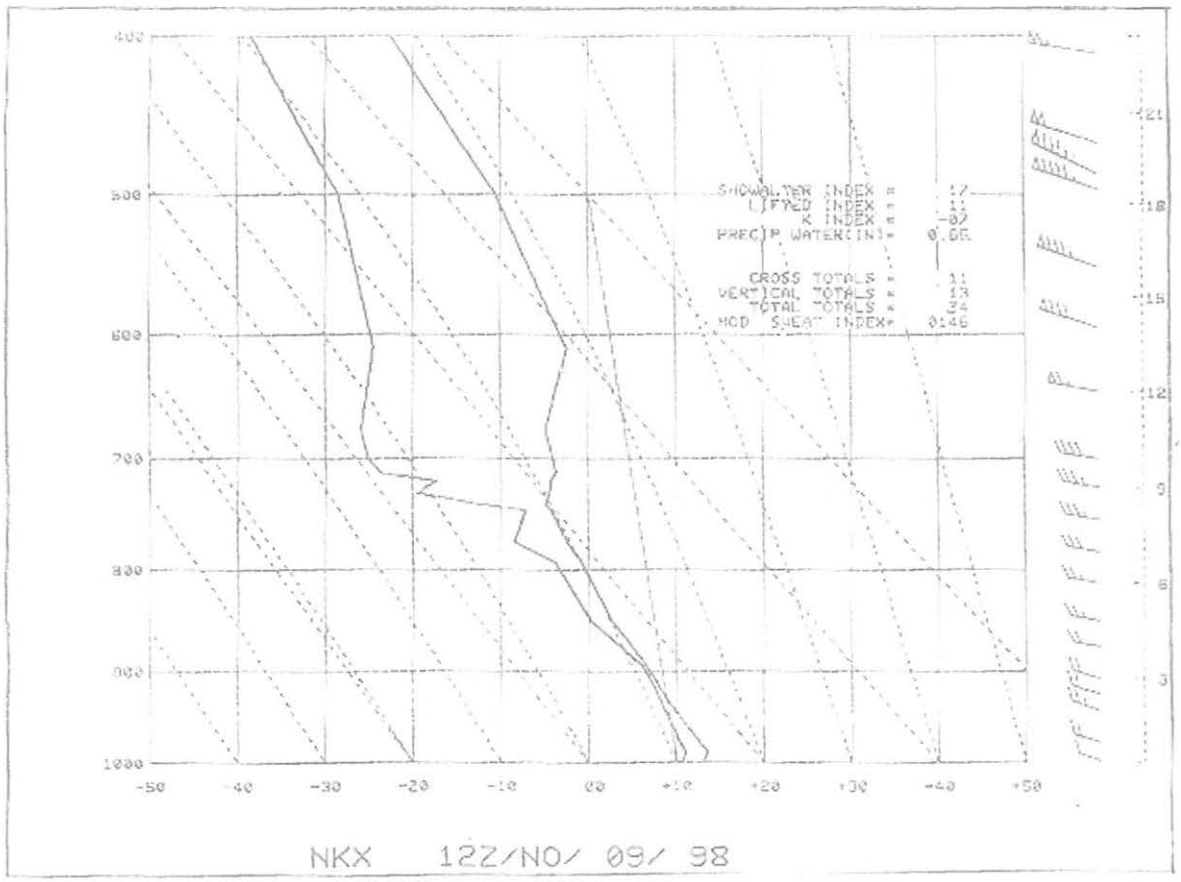

Fig. 19a. 1200 UTC 9 November 1998 KNKX sounding.

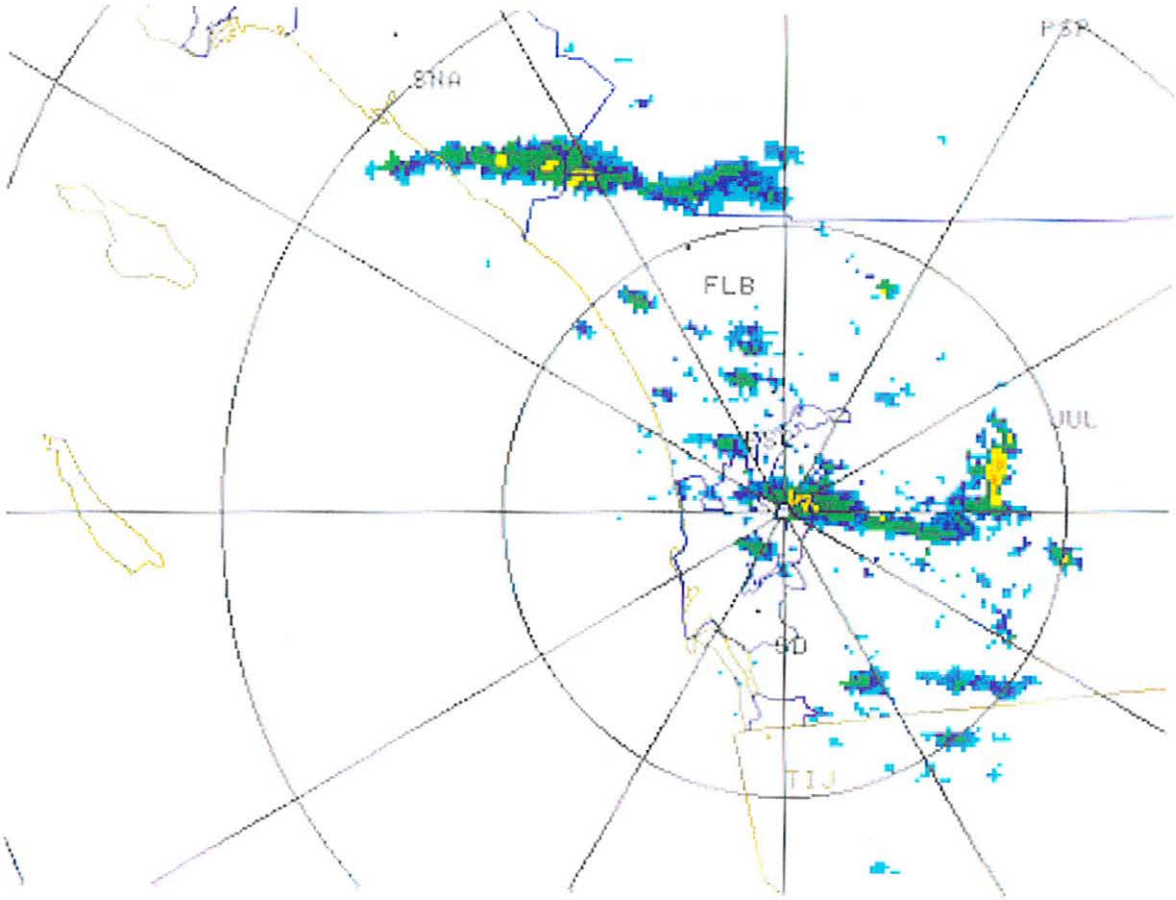

Fig. 19b. 0605 UTC 9 November 1998 KNKX composite reflectivity

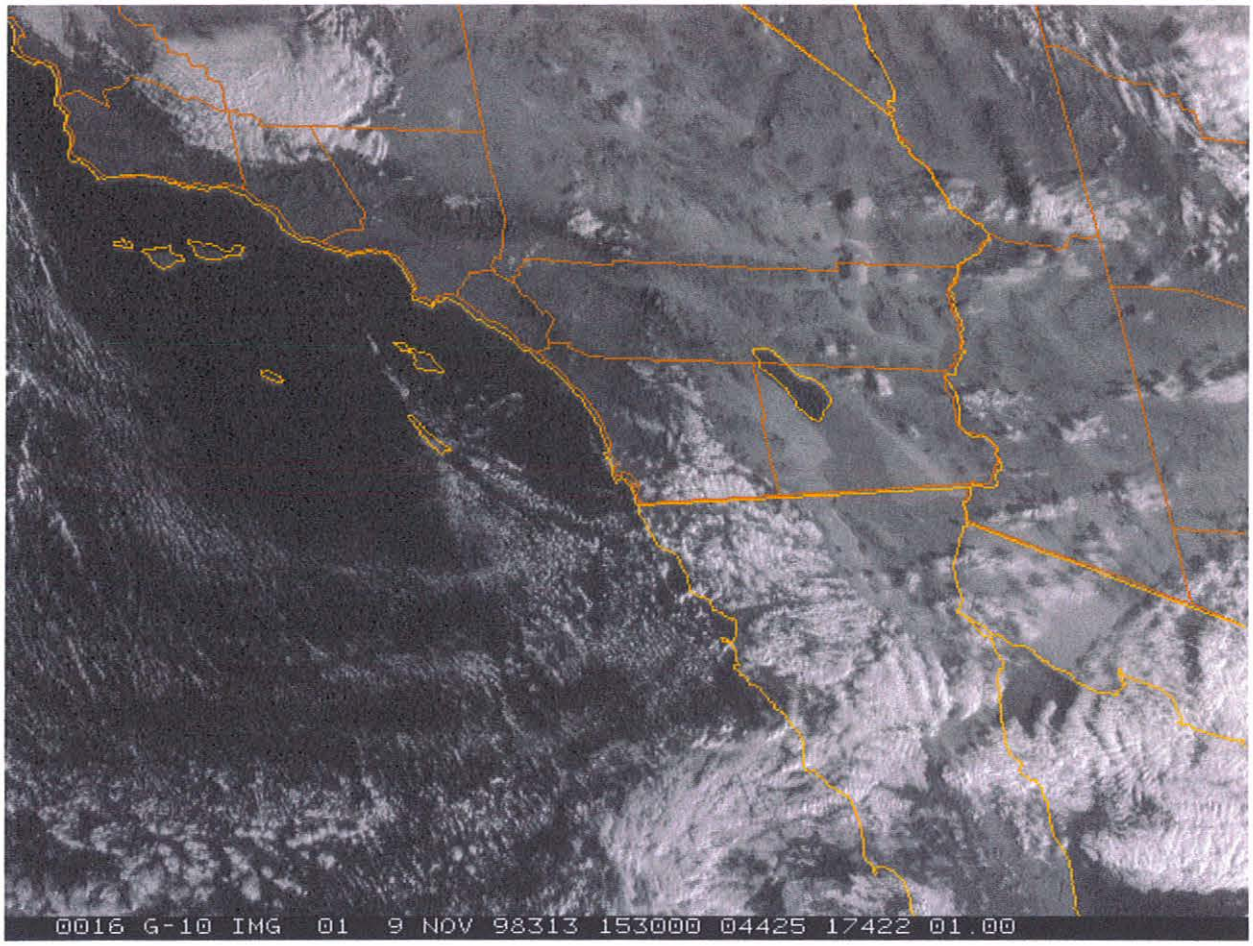

Fig. 20. 1530 UTC 9 November 1998 visible satellite imagery.

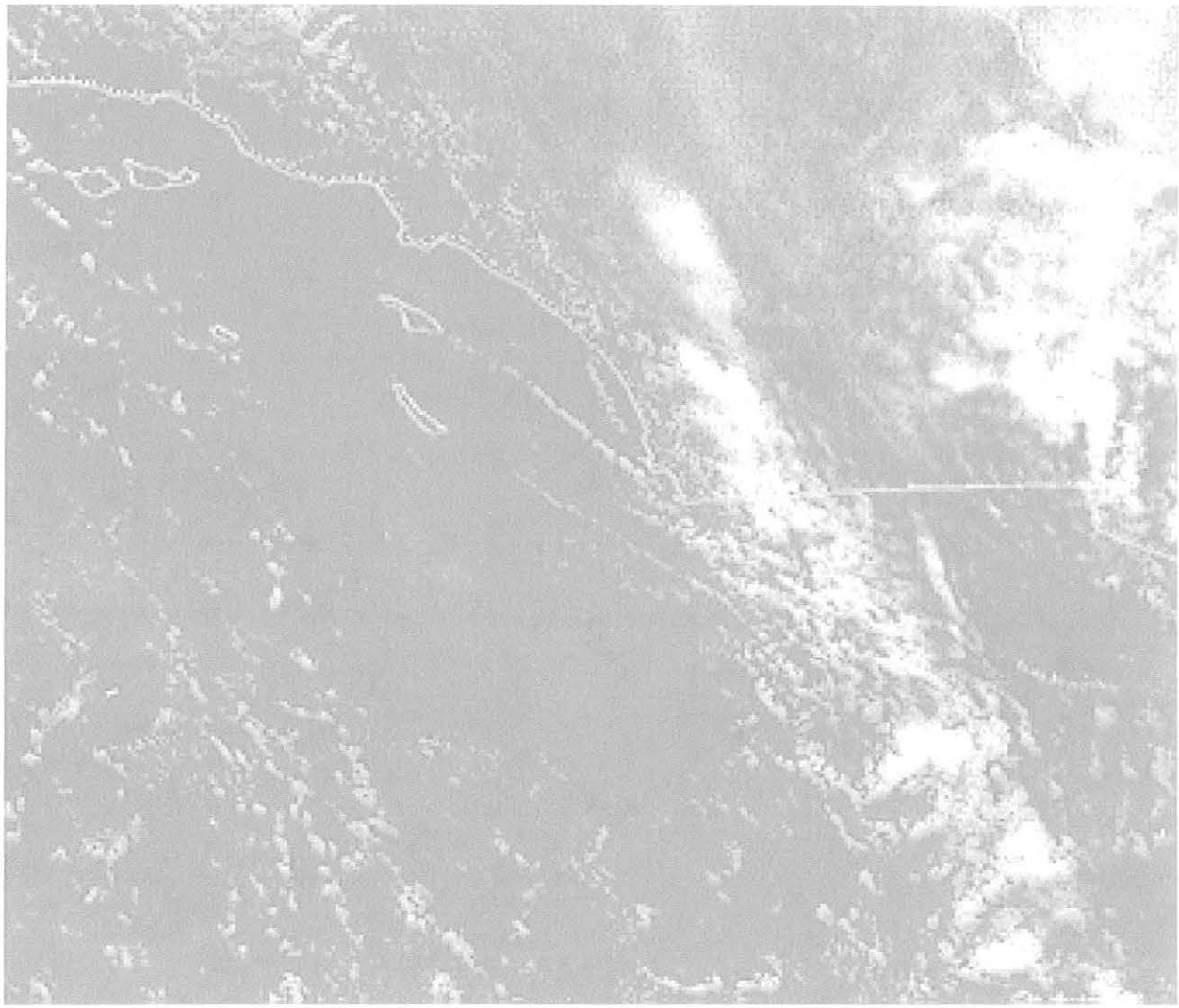

Fig. 21. 2015 UTC 17 February 1998 visible satellite imagery.

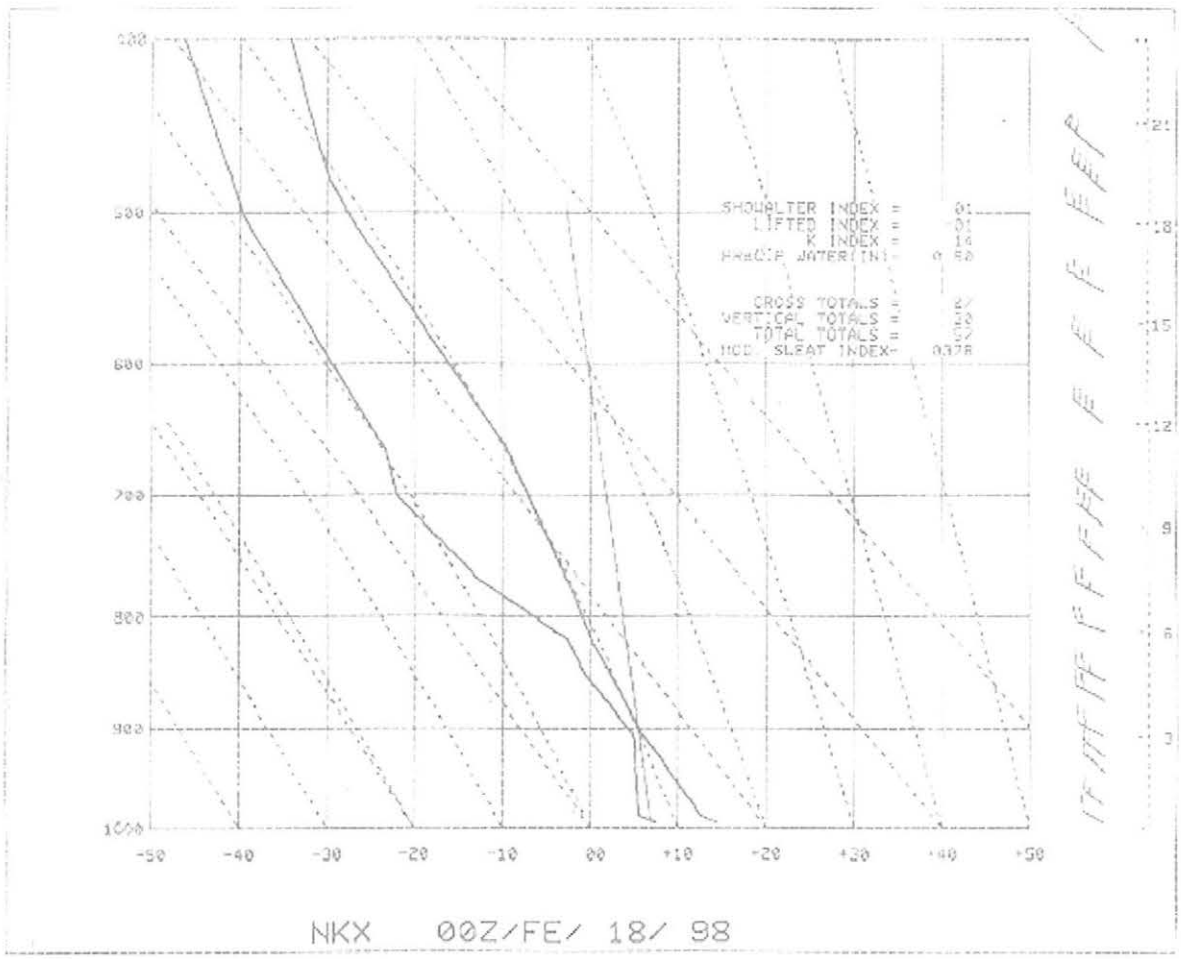

Fig. 22. 0000 UTC 18 November 1998 NKX sounding.

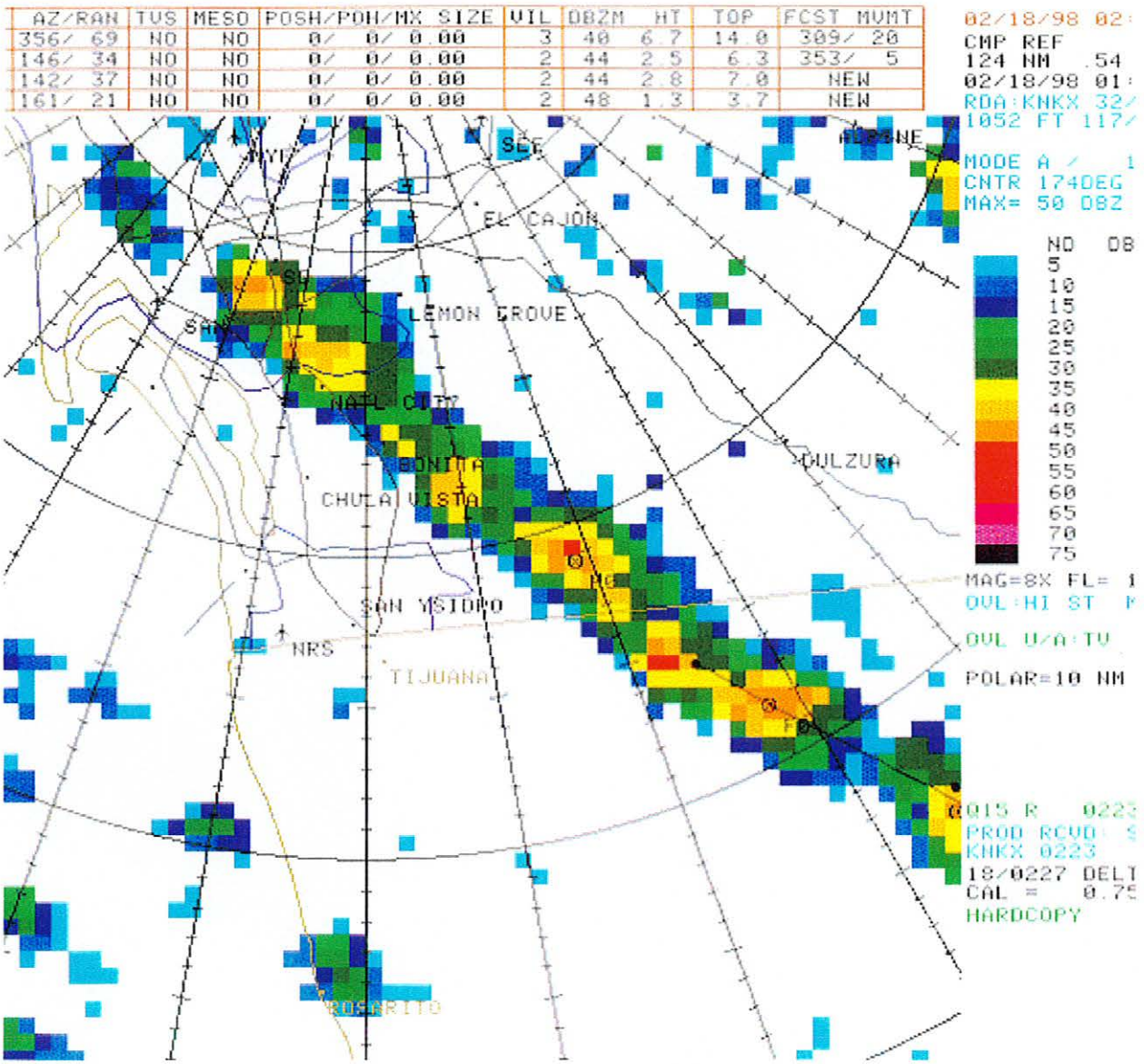

Fig. 23a. 0118 UTC 18 February 1998 KNKX composite reflectivity.

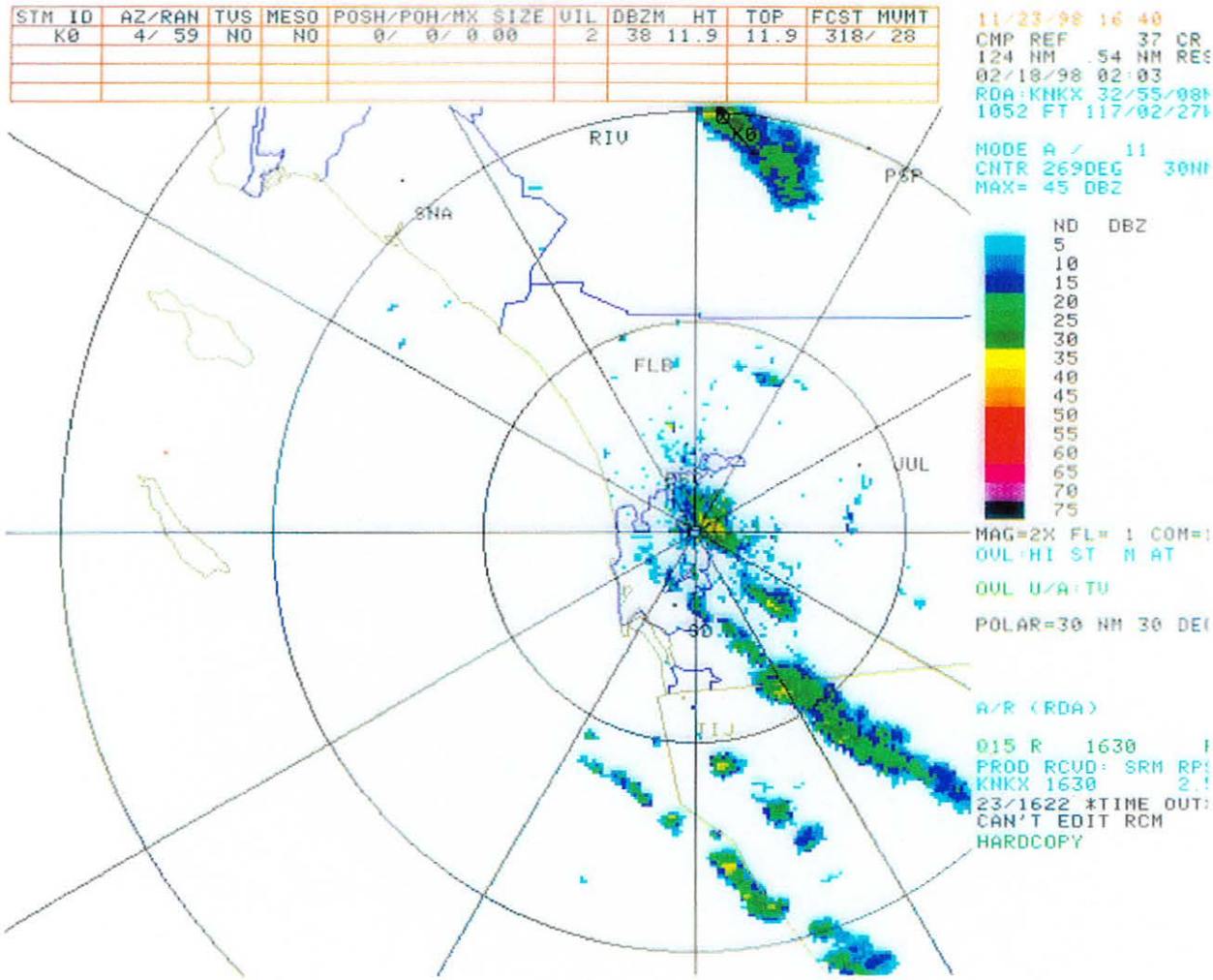

Fig. 23b. 0203 UTC 18 February 1998 KNKX composite reflectivity.

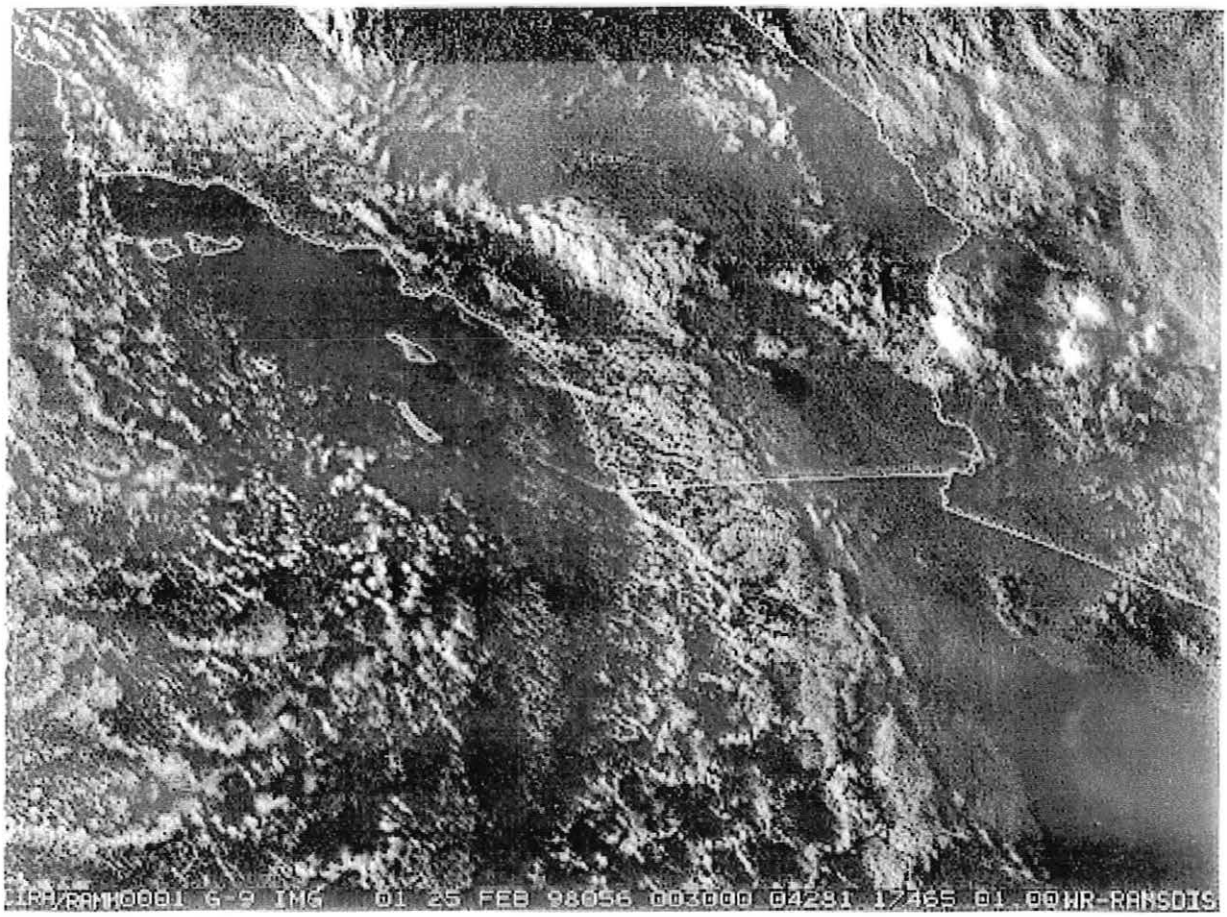

Fig. 24. 0030 UTC 25 February 1998 visible satellite imagery.

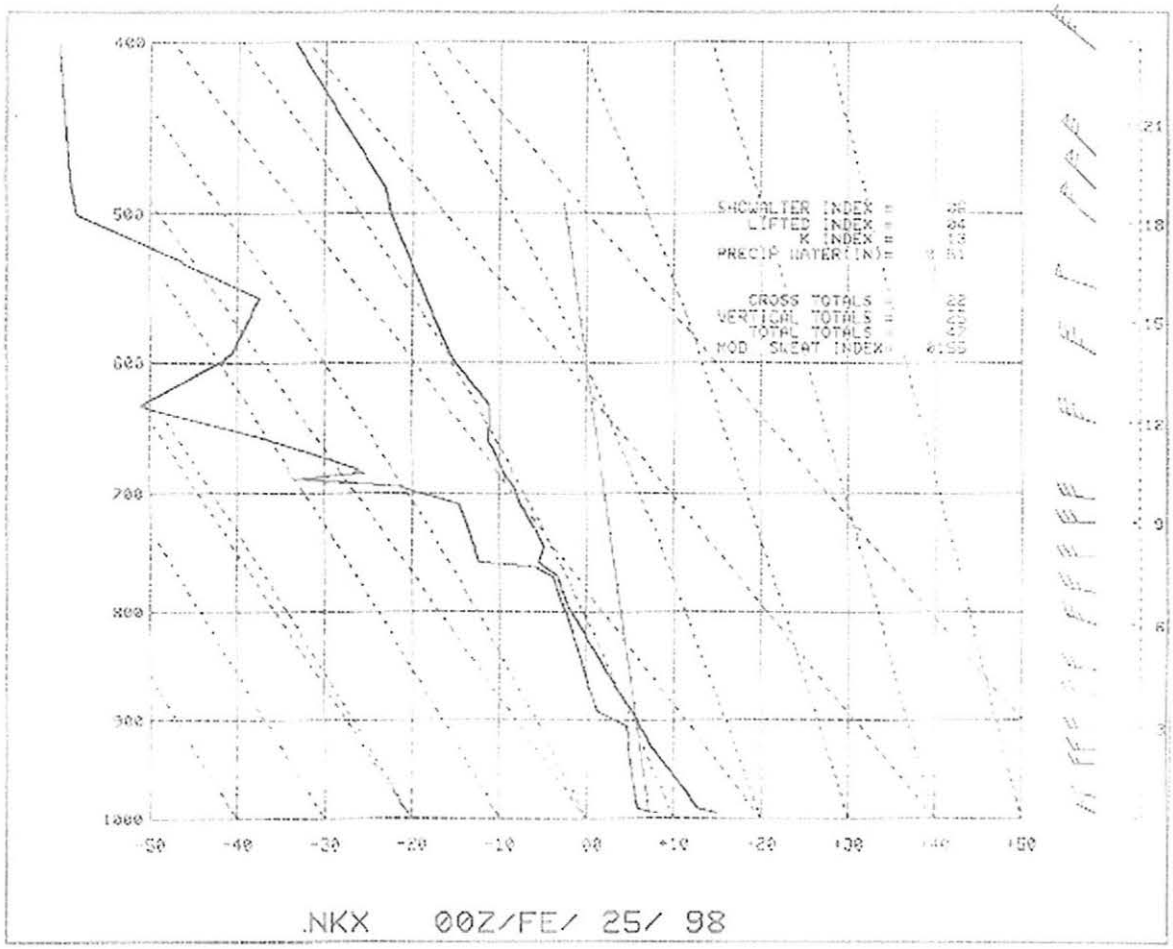

Fig. 25. 0000 UTC 25 February 1998 NKX sounding.

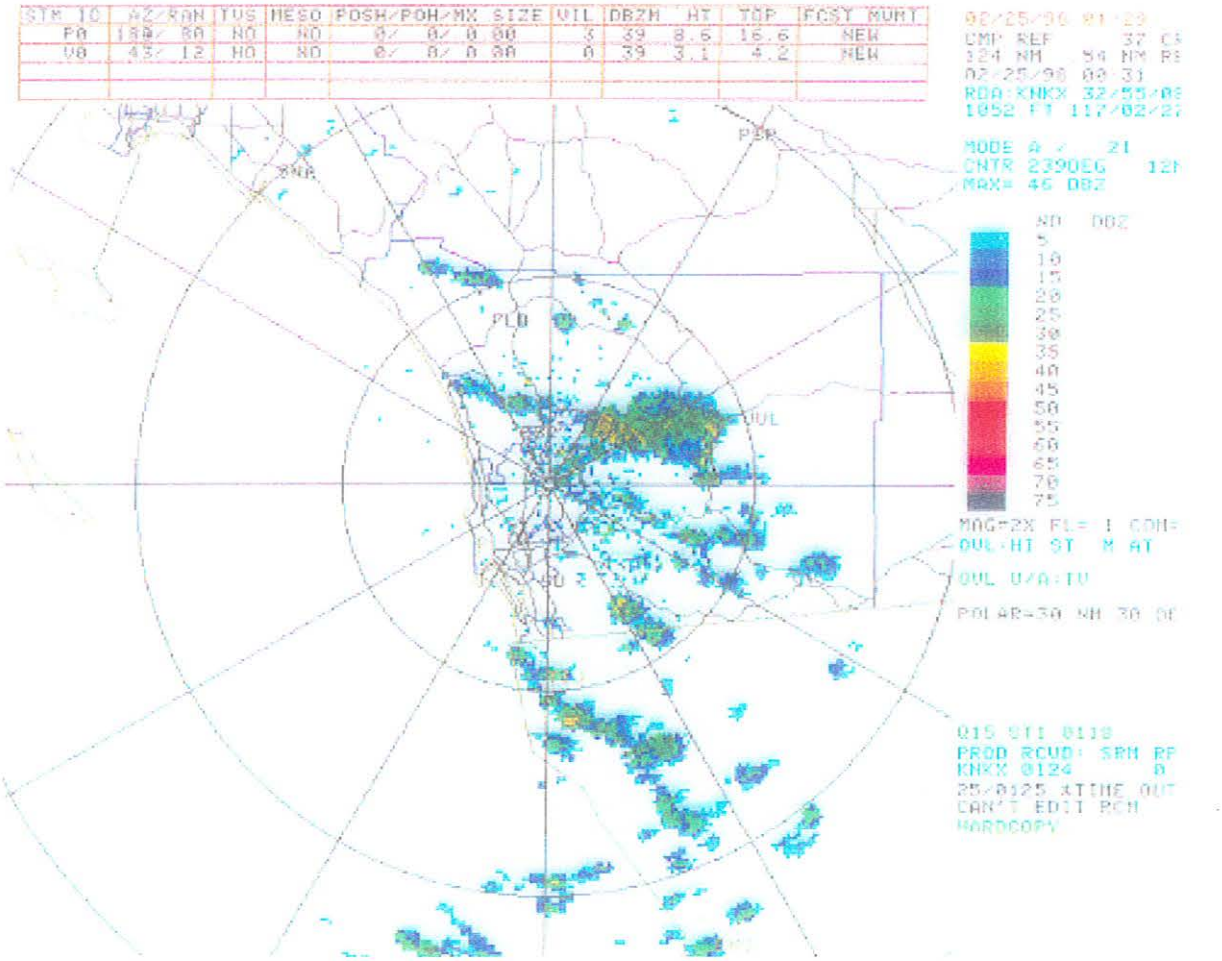

Fig. 26. 0031 UTC 25 February 1998 KNKX composite reflectivity.

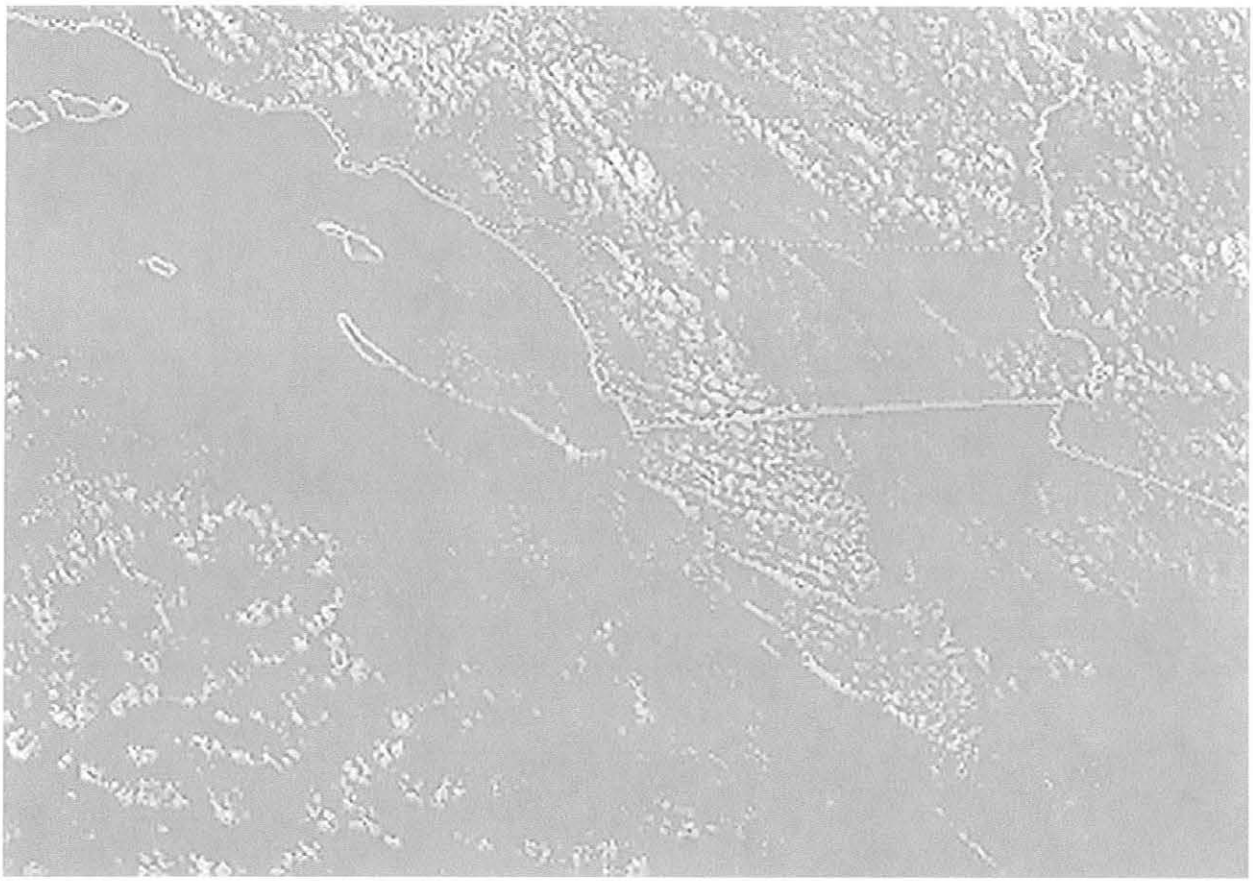

Fig. 27. 2330 UTC 7 April 1998 visible satellite imagery.

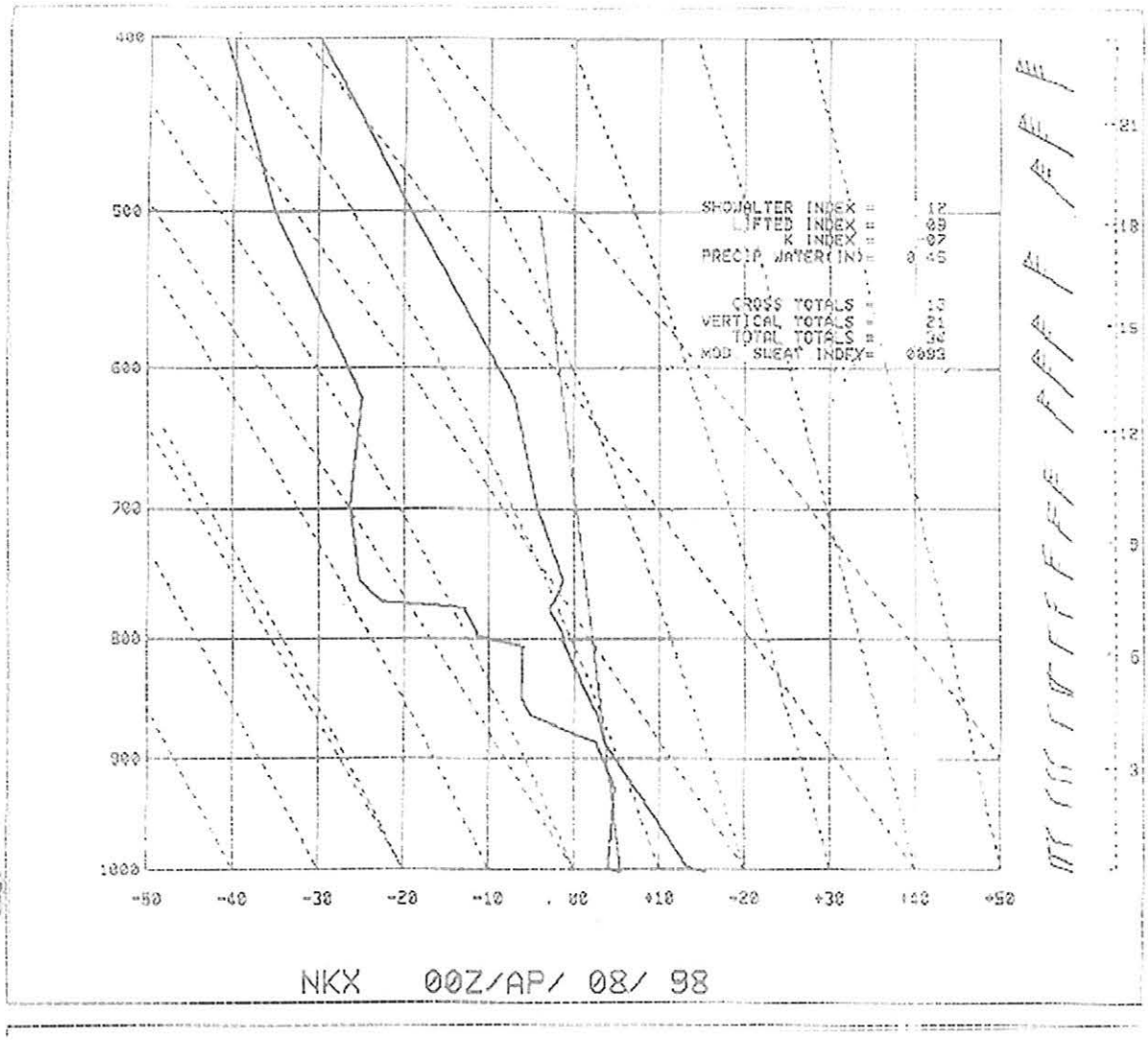

Fig. 28. 0000 UTC 8 April 1998 NKX sounding.

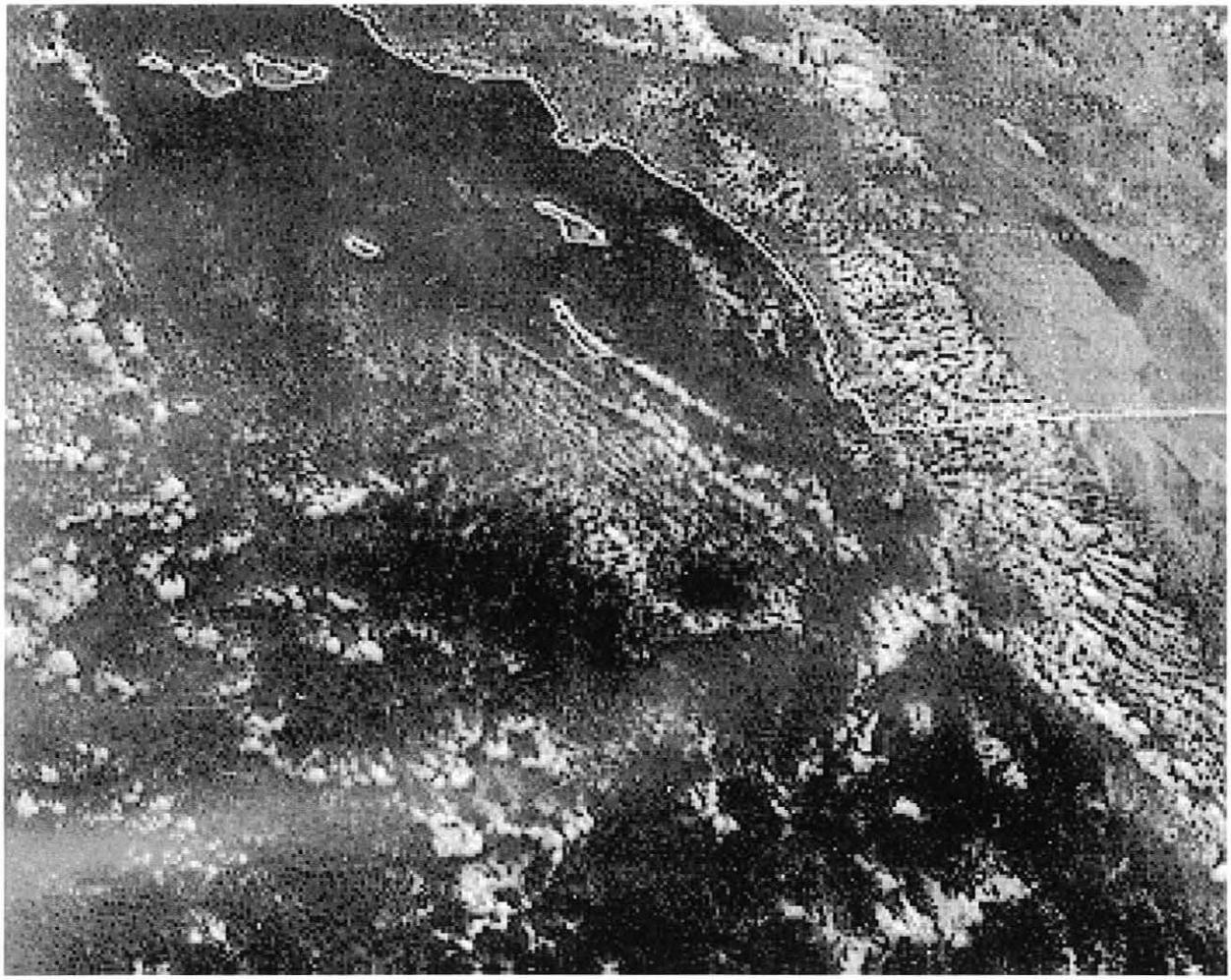

Fig. 29. 2030 UTC 9 February 1998 visible satellite imagery.

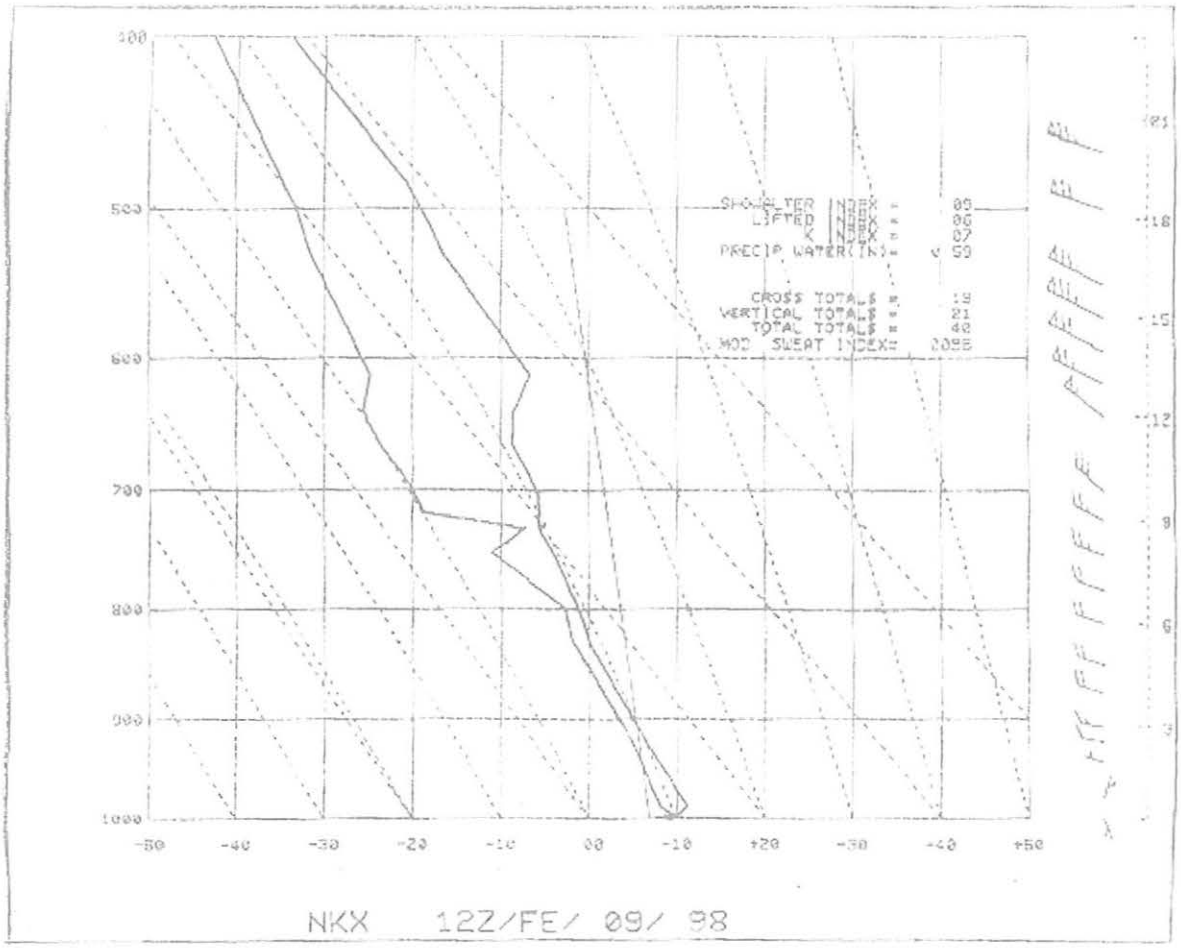

Fig. 30. 1200 UTC 9 February 1998 NKX sounding.

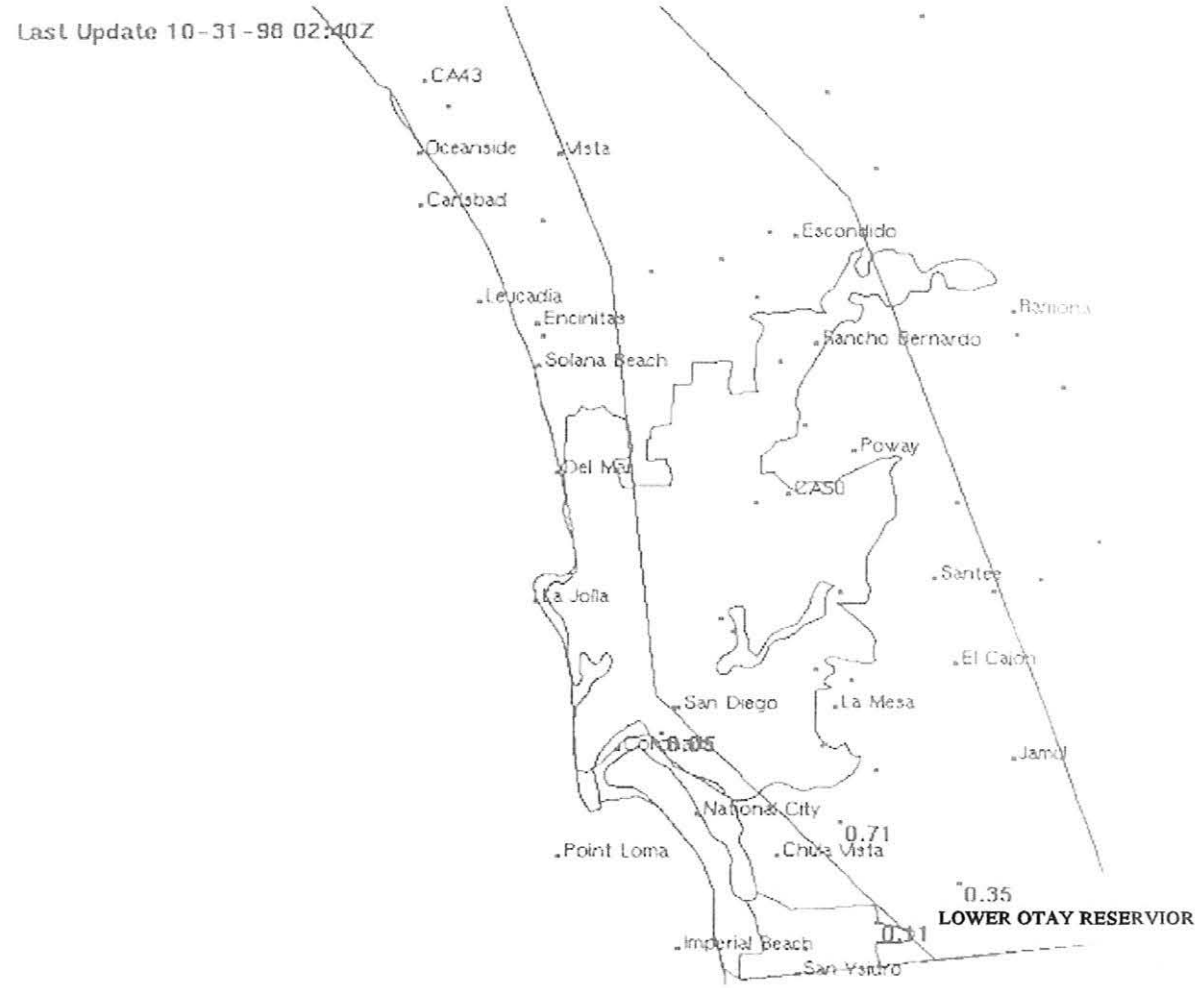

Fig. 31. ALERT hourly precipitation map indicating precipitation between 1200 UTC 30 October 1998 and 1300 UTC 30 October 1998.

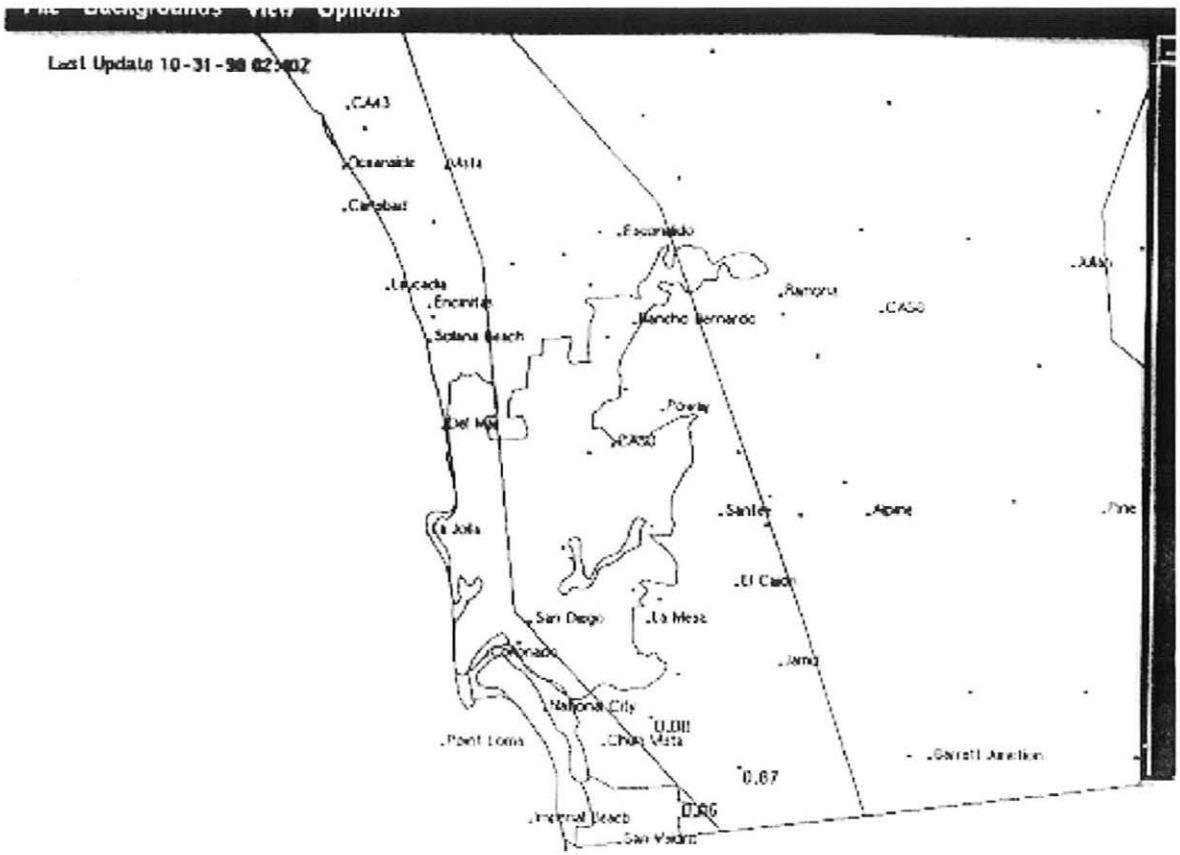

Fig. 32. ALERT hourly precipitation map indicating precipitation between 1300 UTC 30 October 1998 and 1400 UTC 30 October 1998

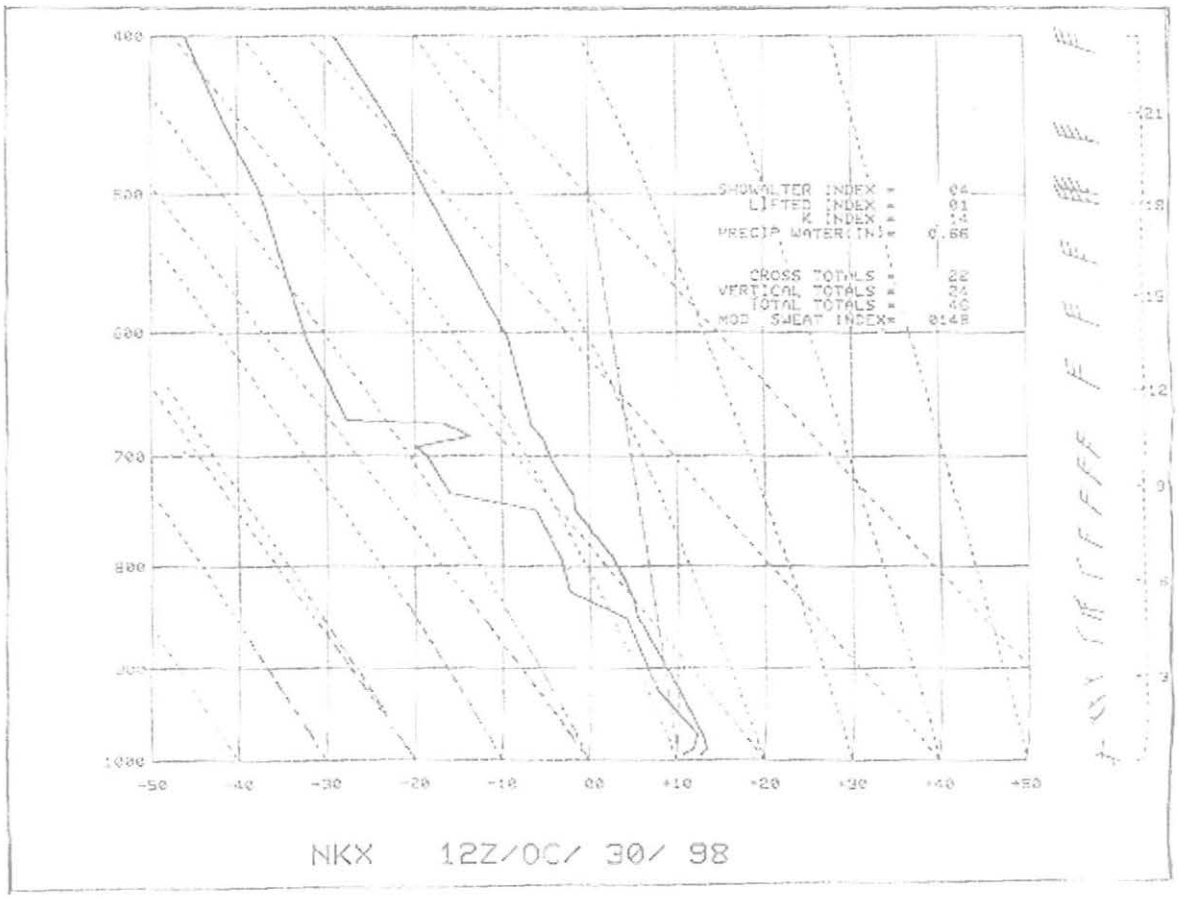

Fig. 33. 1200 UTC 30 October 1998 NKX sounding

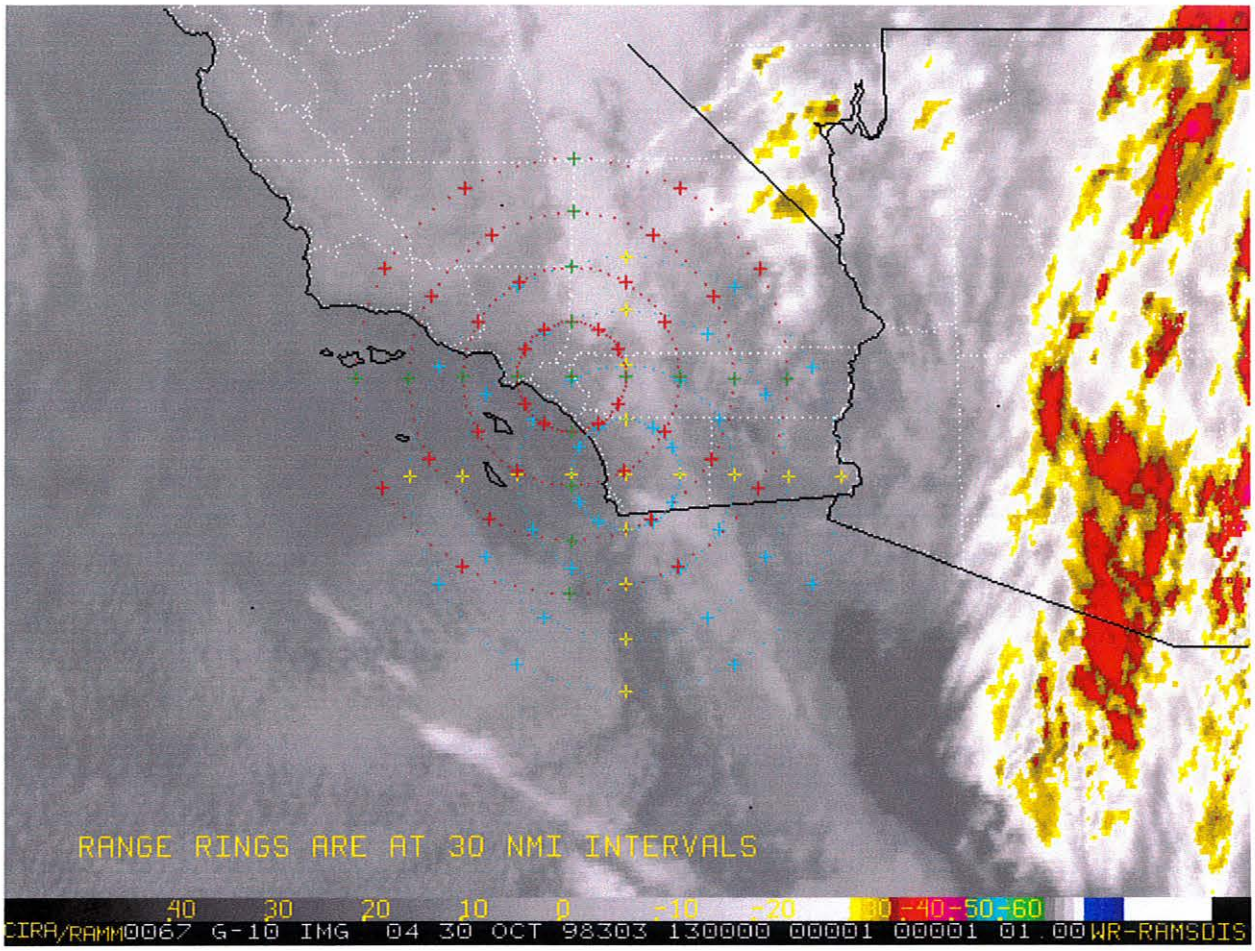

Fig. 34. 1300 UTC 30 October 1998 infrared satellite imagery showing band of precipitation over the Chula Vista/Otay Reservoir area.

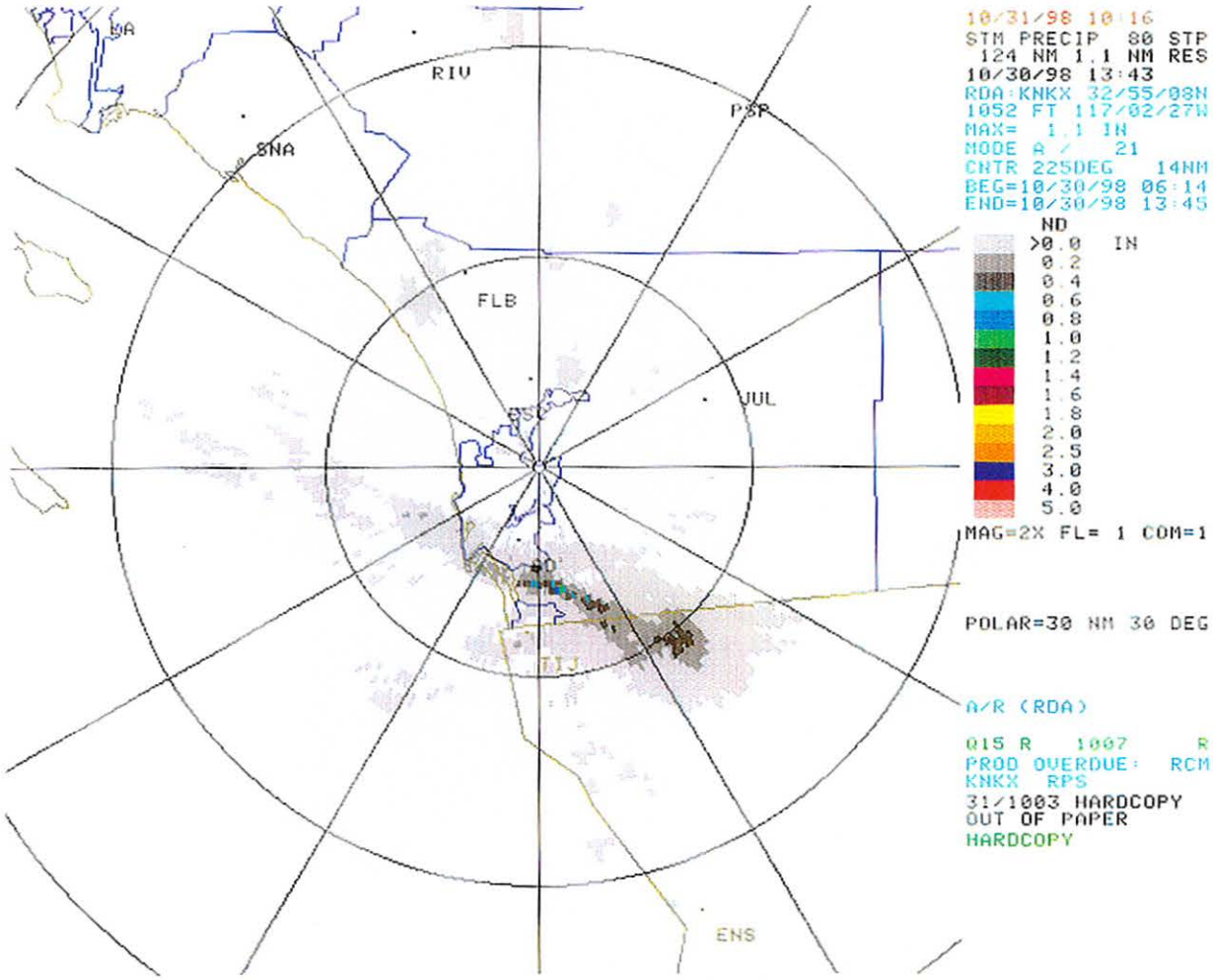

Fig. 35. 1343 UTC 30 October 1998 KNKX Storm Total Precip.

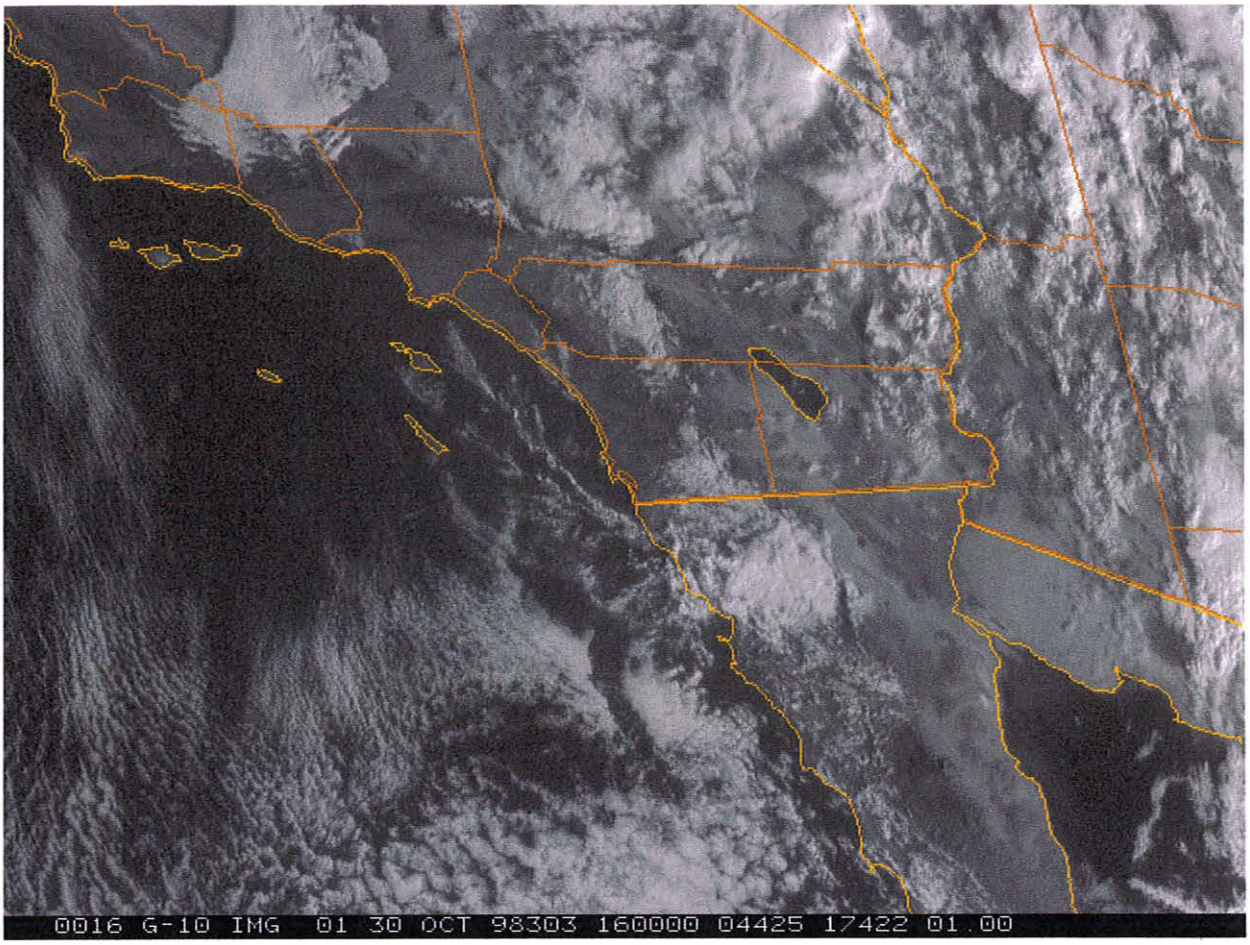

Fig. 36. 1600 UTC 30 October 1998 visible satellite imagery.

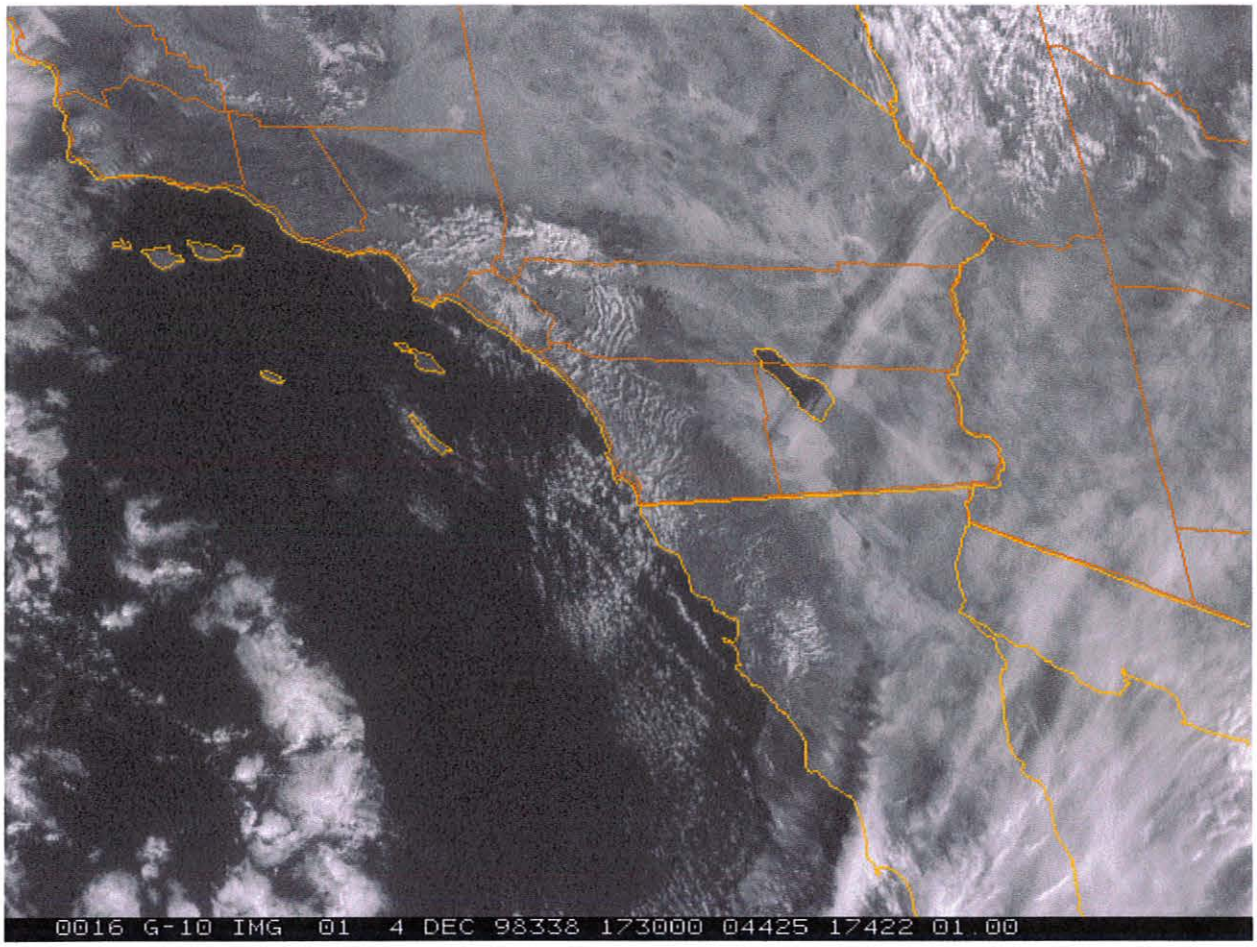

Fig. 37. 1730 UTC 4 December 1998 visible satellite imagery.

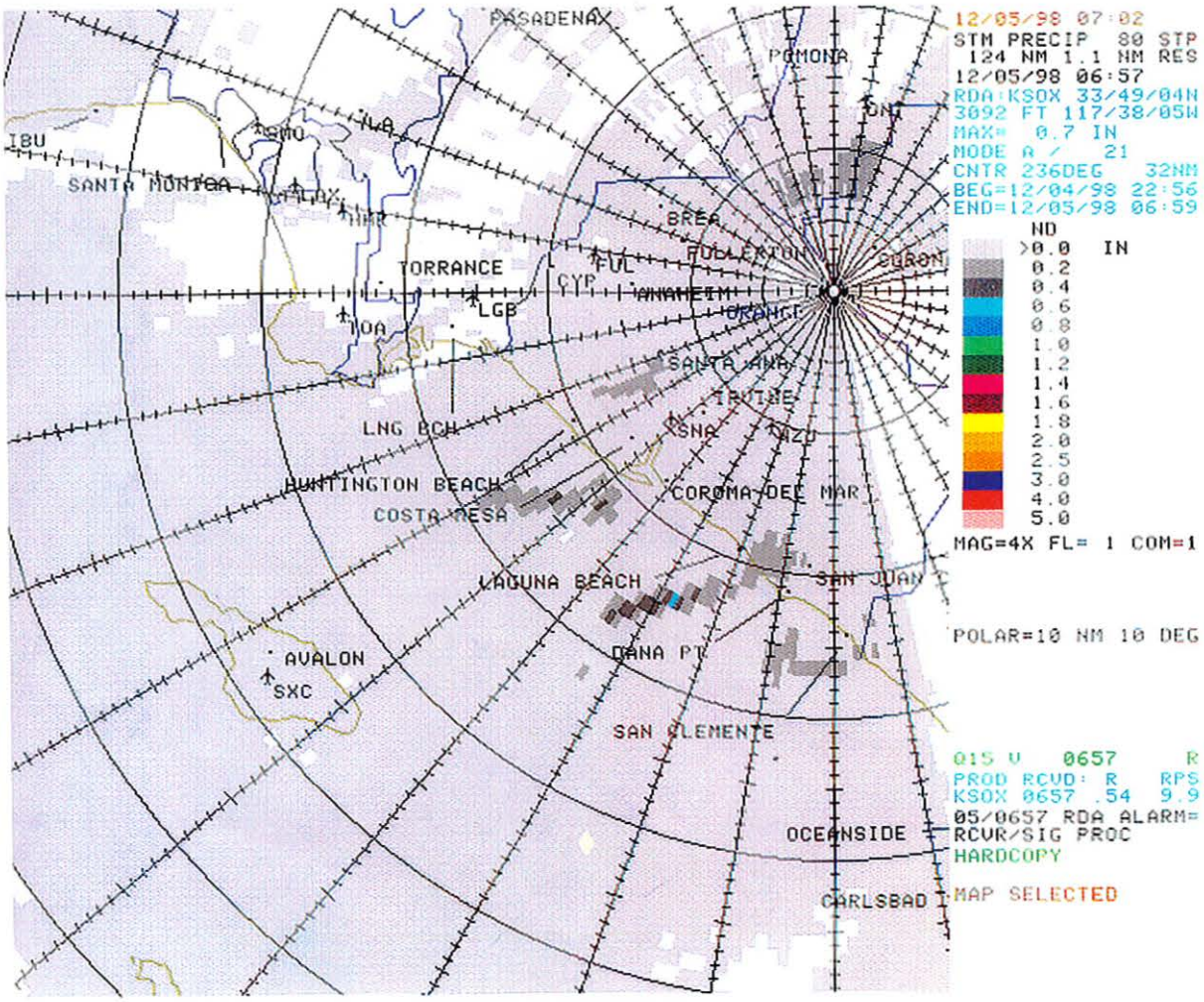

Fig. 38. 0657 UTC 5 December 1998 Storm Total Precip

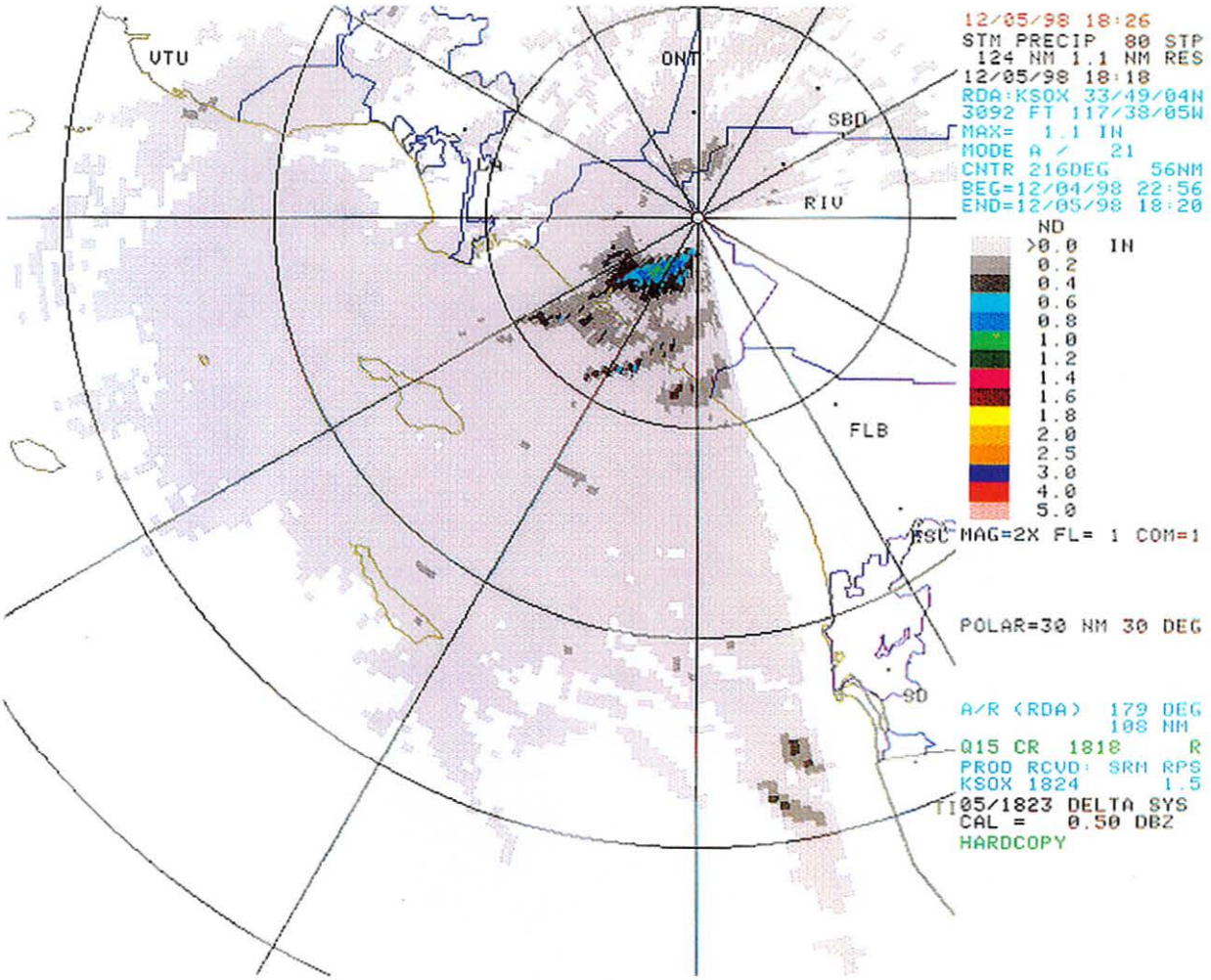

Fig. 39. 1818 UTC 5 December 1998 KSOX Storm Total Precip

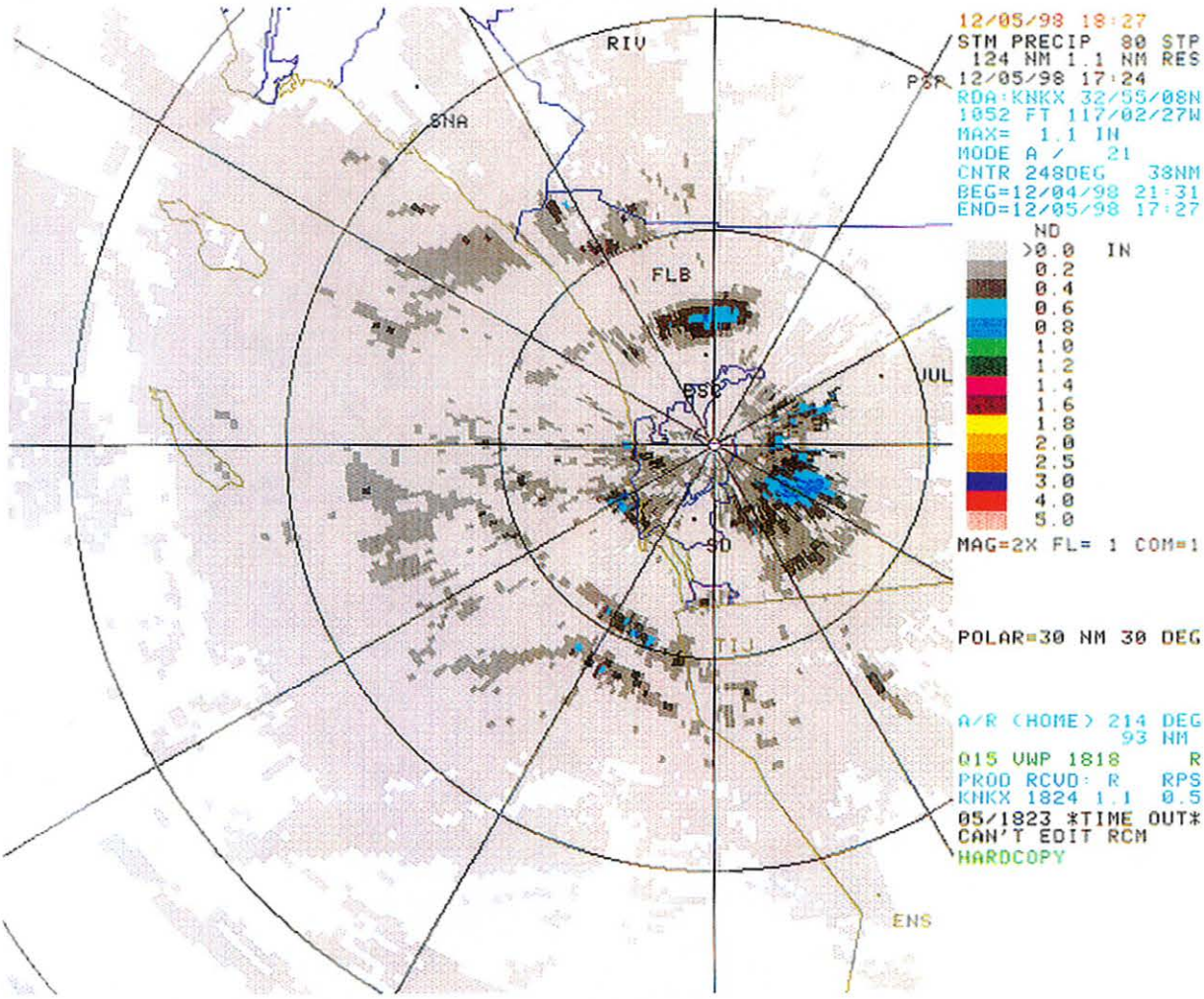

Fig. 40. 1724 UTC 5 December 1998 KNKX Storm Total Precip

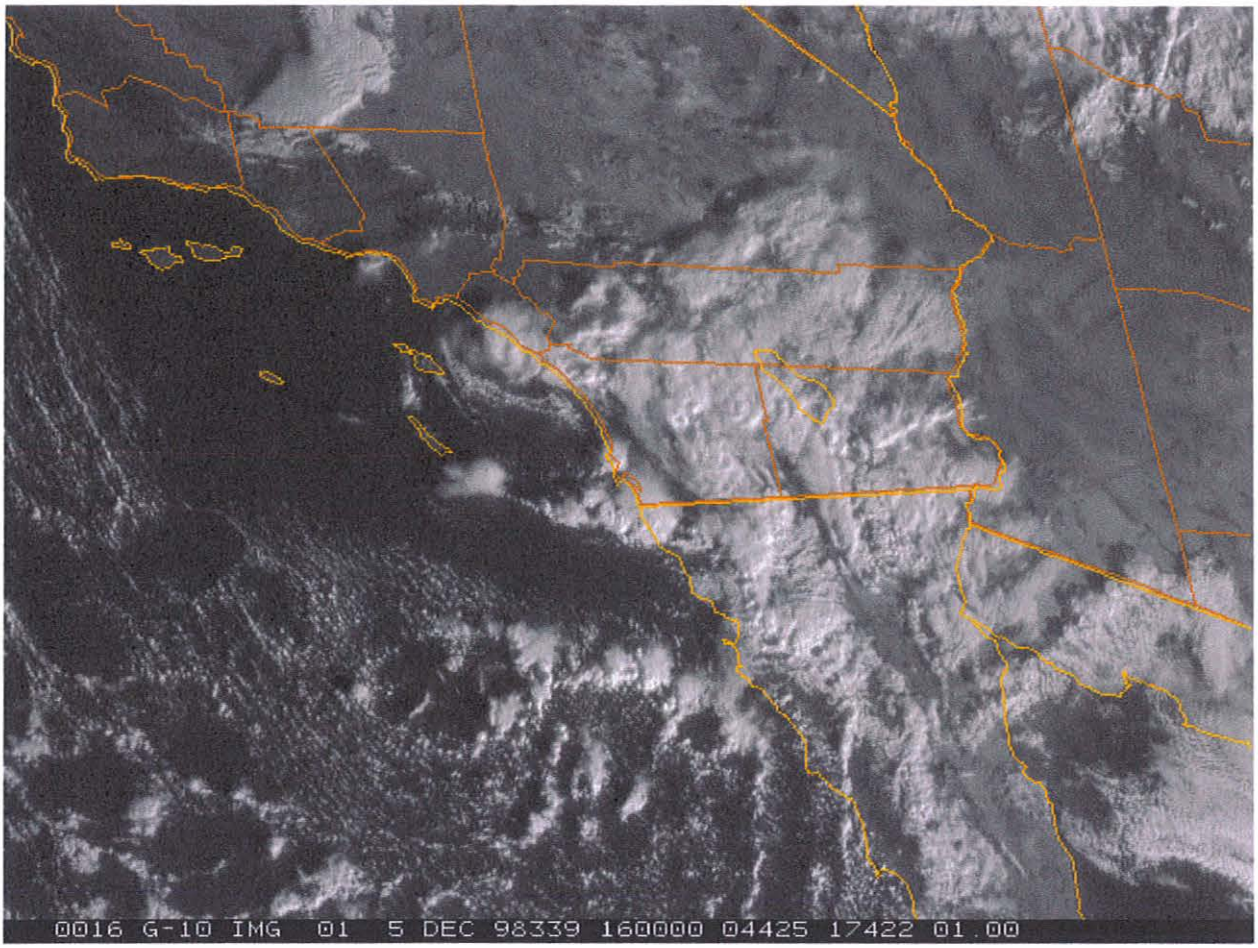

Fig. 41. 1600 UTC 5 December 1998 visible satellite imagery

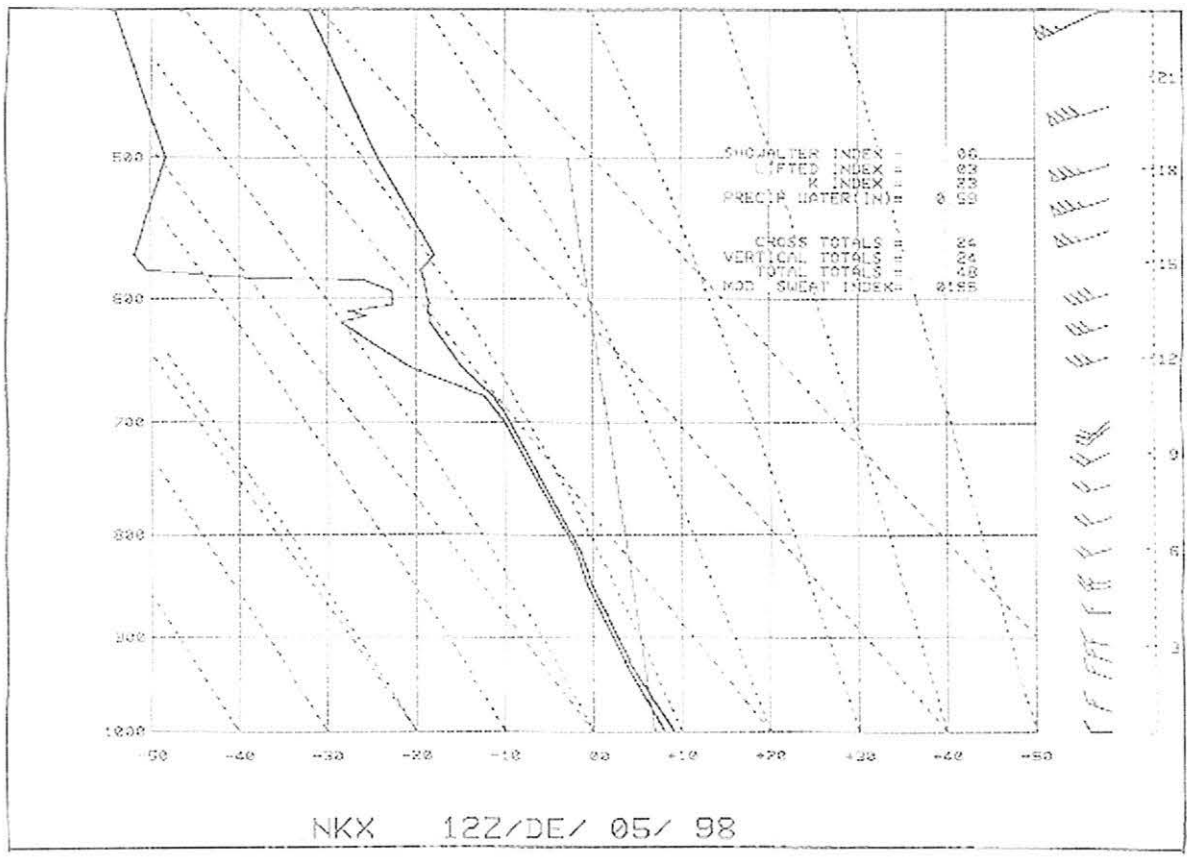

Fig. 42. 1200 UTC 5 December 1998 NKX raob.

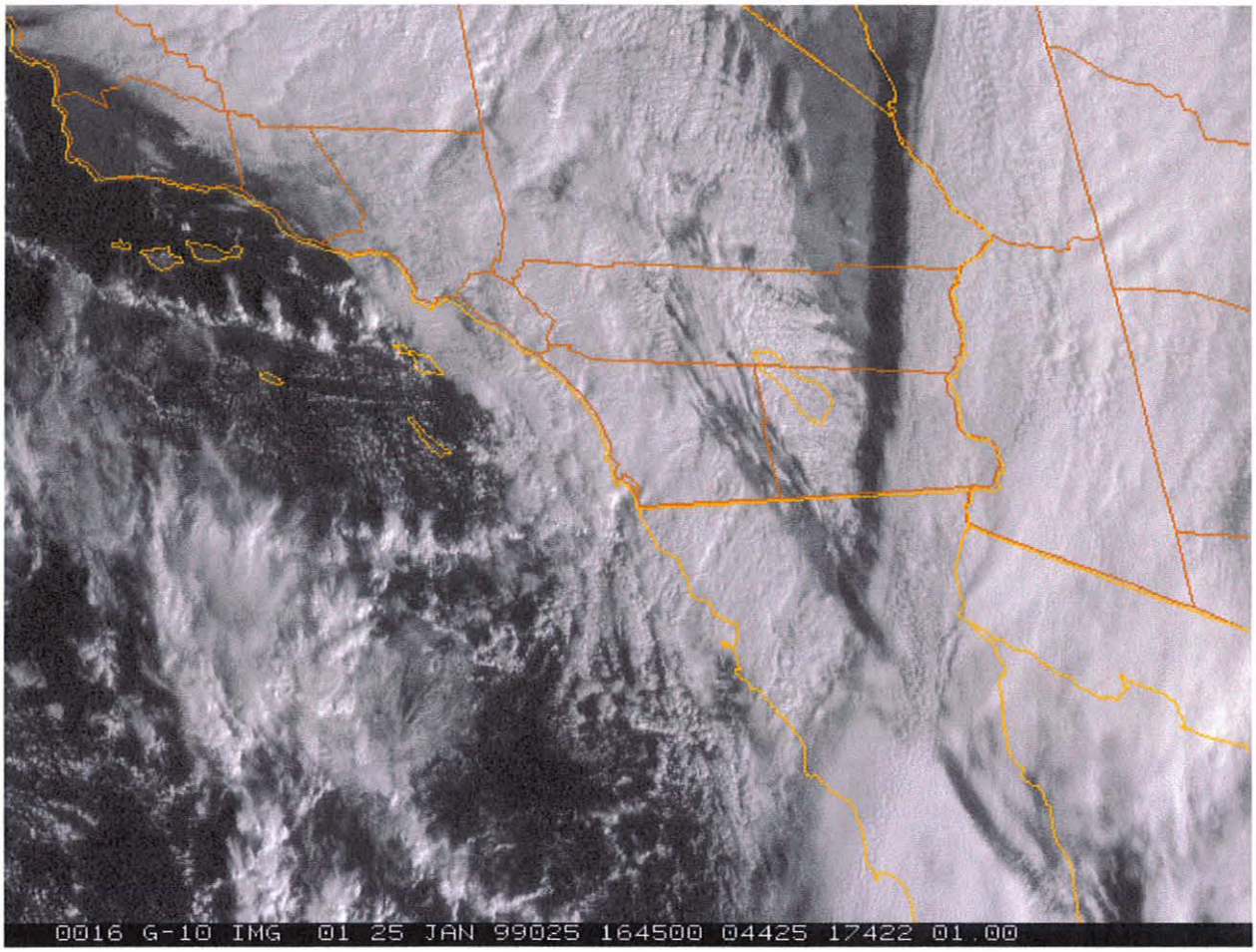

Fig. 43. 1645 UTC 25 January 1999 visible satellite imagery.

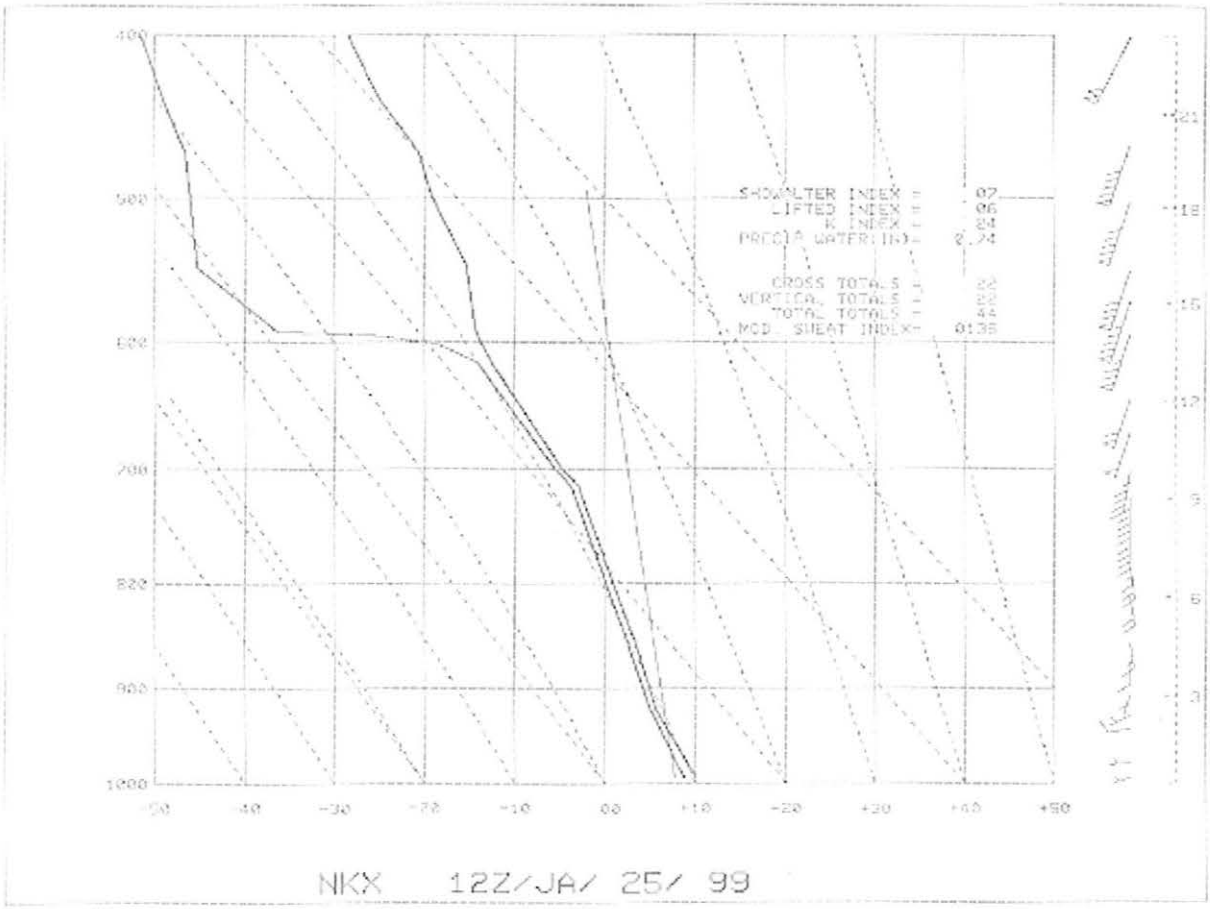

Fig. 44. 1200 UTC 25 January 1999 NKX sounding

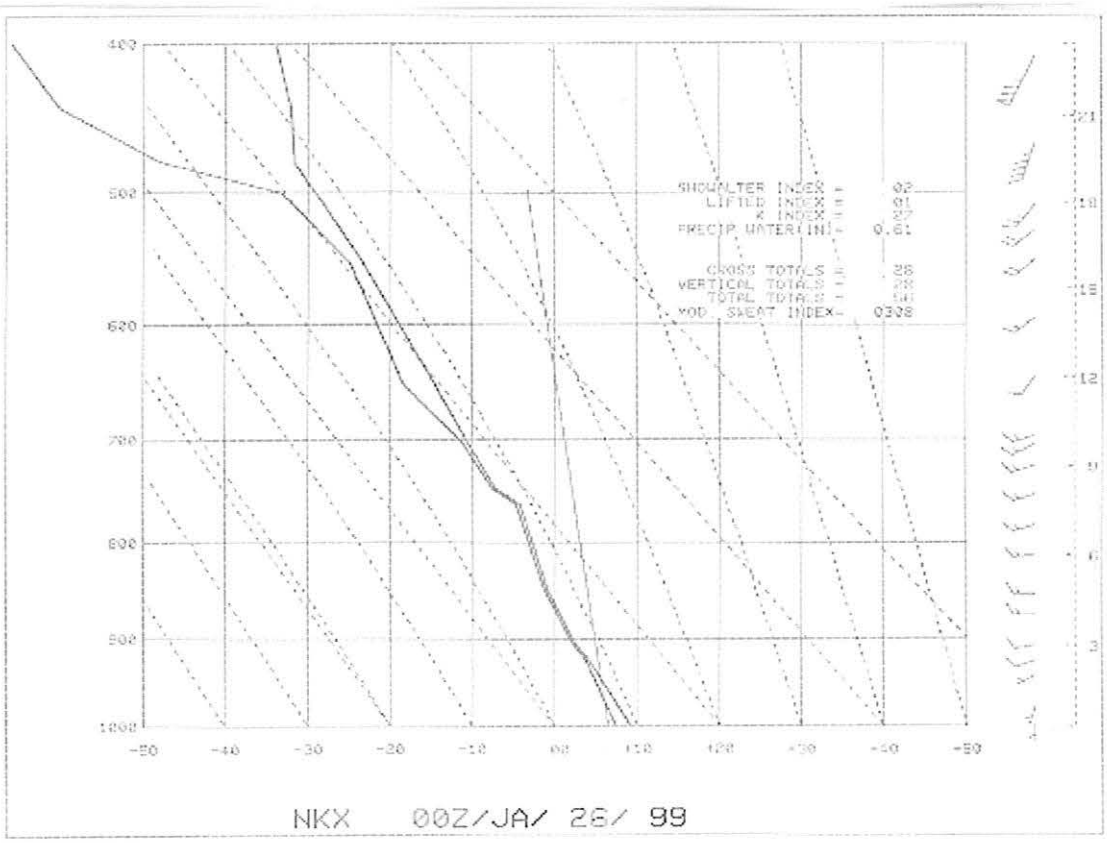

Fig. 45. 0000 UTC 26 January 1999 NKX sounding.

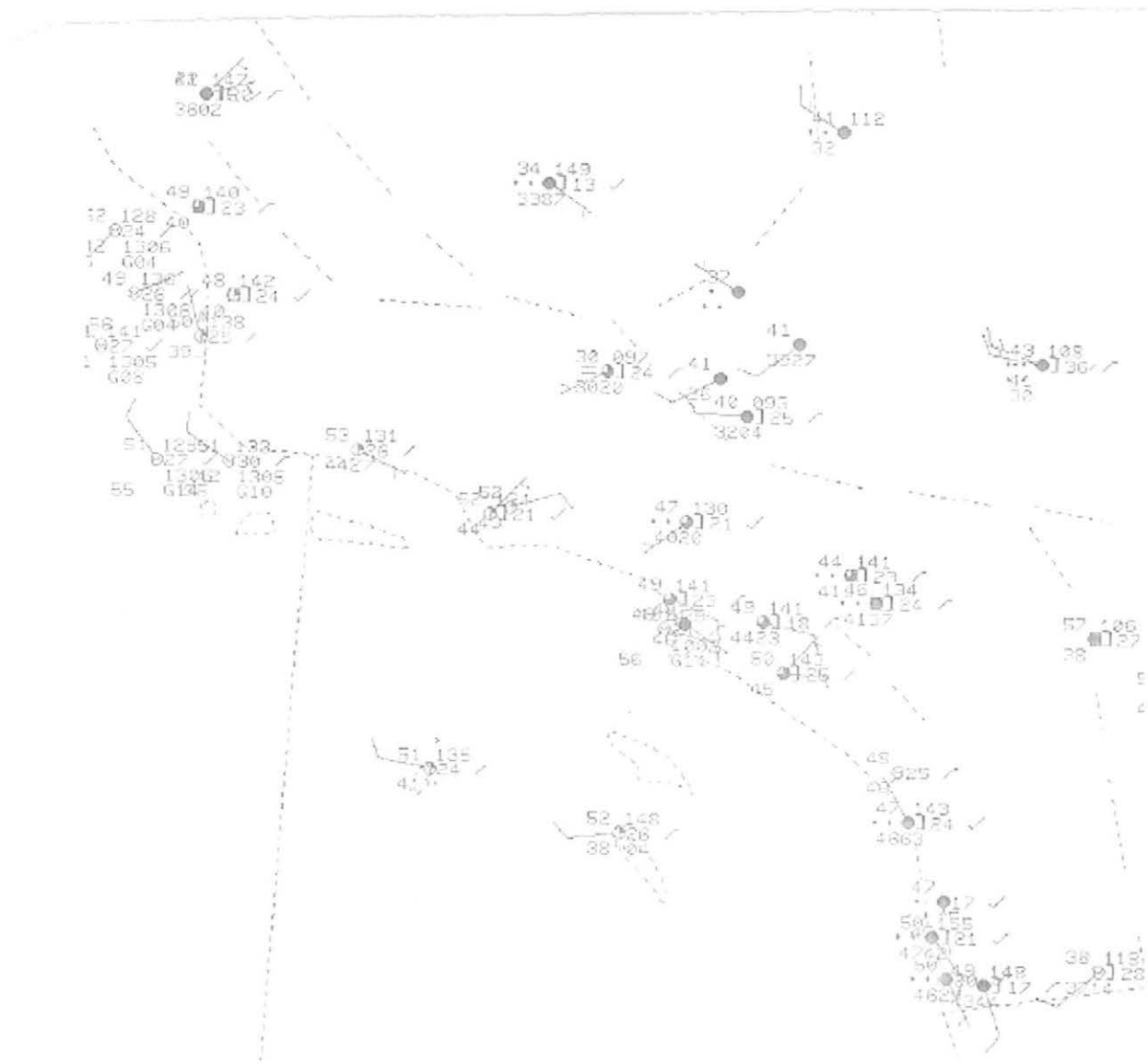

Fig. 46. 1800 UTC 25 January 1999 surface plot.

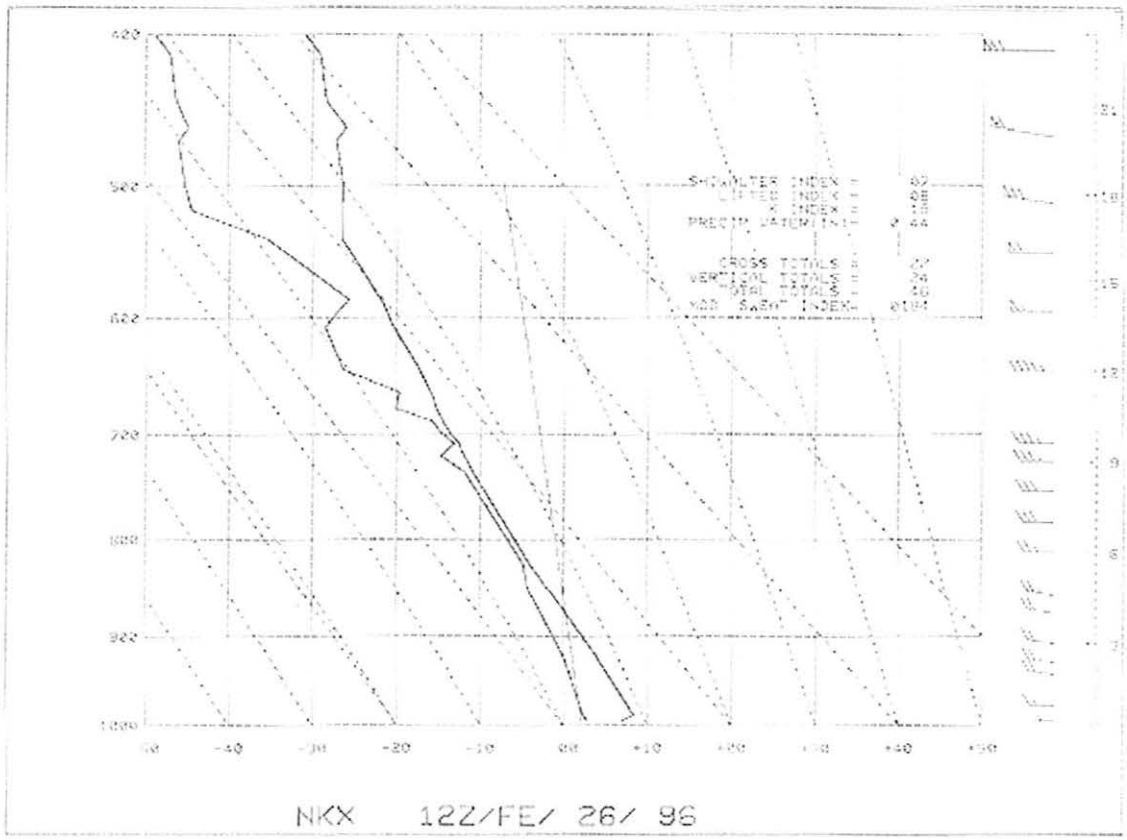

Fig. 47. 1200 UTC 26 February 1996 NKX sounding.

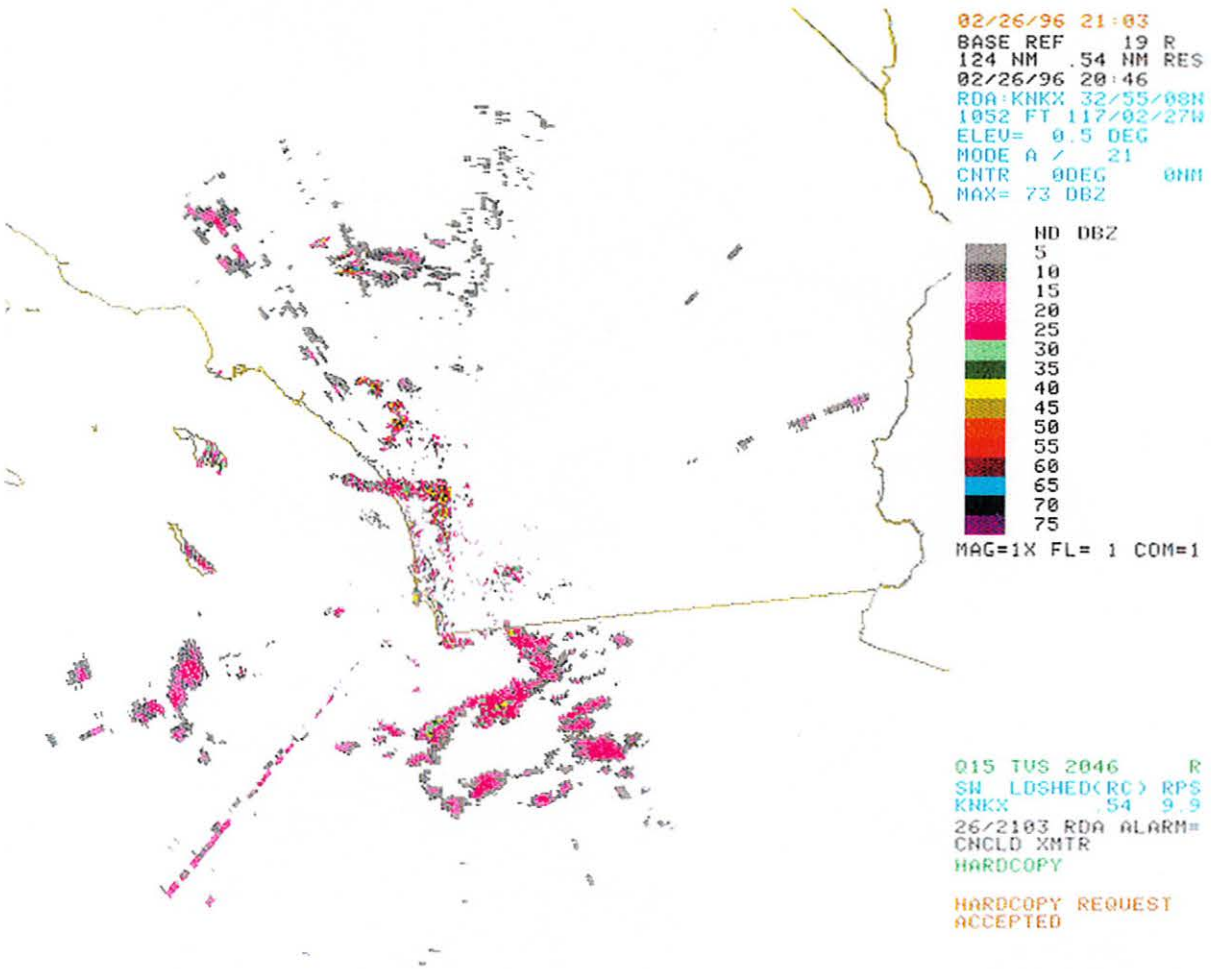

Fig. 48. 2046 UTC 26 February 1996 Composite Reflectivity.